

# Localization for Ground Robots: On Manifold Representation, Integration, Re-Parameterization, and Optimization

Mingming Zhang<sup>†</sup>, Xingxing Zuo<sup>†</sup>, Yiming Chen, and Mingyang Li

{ mingmingzhang, xingxingzuo, yimingchen, mingyangli }@alibaba-inc.com  
A.I. Labs, Alibaba Group, Hangzhou, China

**Abstract**—In this paper, we focus on localizing ground robots, by probabilistically fusing measurements from the wheel odometry and a monocular camera. For ground robots, the wheel odometry is widely used in localization tasks, especially in applications under planar-scene based environments. However, since the wheel odometry only provides 2D motion estimates, it is extremely challenging to use that for performing accurate full 6D pose (3D position and 3D rotation) estimation. Traditional methods on 6D localization either approximate sensor or motion models, at a cost of accuracy reduction, or rely on other sensors, e.g., inertial measurement unit (IMU), to obtain full 6D motion. By contrast, in this paper, we propose a novel probabilistic framework that is able to use the wheel odometry measurements for high-precision 6D pose estimation, in which only the wheel odometry and a monocular camera are mandatory<sup>1</sup>. Specifically, we propose novel methods for i) formulating a motion manifold by parametric representation, ii) performing manifold based 6D integration with the wheel odometry measurements, and iii) re-parameterizing manifold equations periodically for error reduction. Finally, we propose a complete localization algorithm based on a manifold-assisted sliding-window estimator, fusing measurements from the wheel odometry, a monocular camera, and optionally an IMU. By extensive simulated and real-world experiments, we show that the proposed algorithm outperforms a number of state-of-the-art vision based localization algorithms by a significant margin, especially when deployed in large-scale complicated environments.

## I. INTRODUCTION

The localization problem for ground robots has been under active research and development for a couple of decades [1] [2] [3] [4] [5] [6] [7]. The most mature technique of localizing ground robots in large-scale environment is the one that relies on high-quality GPS-INS systems together with 3D laser range-finders [3] [8] [9] [10]. This design is widely used in autonomous driving vehicles to provide precise pose estimates for scene understanding, path planing, and decision [10]. However, those systems are at high manufacturing and maintenance costs, requiring thousands or even tens or hundreds of thousands of dollars, which inevitably prevent their wide applications. Alternatively, low-cost localization approaches have gained increased interests in recent years, especially the ones that rely on cameras [4] [11]. Camera’s size, low cost, and 3D sensing capability makes itself a popular sensor. Additionally, since IMU and camera sensors have complementary characteristics, when used together with an IMU, the accuracy and robustness of vision-based localization can

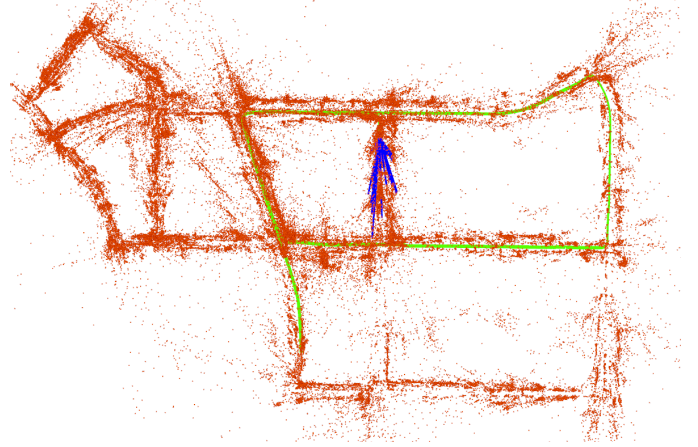


Fig. 1: Representative visualization of the proposed algorithm. Top: An image from urban28 of KAIST [19] used for visual localization. Bottom: visual localization using the proposed algorithm, green line represents the estimated trajectory, red dots denote the positions of visual landmarks from a map, and blue lines represent landmark-to-feature correspondences.

be significantly improved [12] [13] [14] [15] [16] [17] [18]. In fact, camera-IMU localization<sup>2</sup> is widely used in real commercial applications, e.g., smart drones, augmented and virtual reality headsets, or mobile phones.

However, all localization methods mentioned above are *not* optimized for ground robots. Although camera-IMU localization generally performs better than camera only localization by resolving the ambiguities in estimating scale, roll, and pitch [12] [14] [20], it has its own limitations when used for localizing ground robots. Firstly, there are a couple of degenerate cases that can result in large errors when performing motion

<sup>†</sup>Mingming Zhang and Xingxing Zuo contribute equally to this work.

<sup>1</sup>Other sensors, e.g. an IMU, can be used for further improving the system accuracy. However those are not mandatory sensors in our proposed algorithm.

<sup>2</sup>Camera-IMU localization can also be termed as vision-aided inertial navigation, visual-inertial odometry (VIO), or visual inertial navigation system (VINS) in other papers.

estimation, e.g., system under static motion, zero rotational velocity motion, constant local linear acceleration motion, and so on [12] [21] [22]. The likelihood of encountering those degenerate cases on ground robots is significantly larger than that on hand-held mobile devices. Secondly, unlike drones or smart headset devices which move freely in 3D environment, ground robots can only move on a manifold (e.g., ground surfaces) due to the nature of their mechanical design. This makes it possible to use additional low-cost sensors and derive extra mathematical constraints for improving the localization performance [6] [21].

When looking into the literature and applications of ground robot localization, wheel odometry is a widely used sensor system, for providing 2D linear and rotational velocities. Compared to IMUs, wheel odometry has two major advantageous factors in localization. On one hand, wheel odometry provides linear velocity directly, while IMU measures gravity affected linear accelerations. Integrating IMU measurements to obtain velocity estimates will inevitably suffer from measurement errors, integration errors, and state estimation errors (especially about roll and pitch). On the other hand, errors in positional and rotational estimates by integrating IMU measurements are typical a function of time. If a robot moves slowly for a short distance during a long time period, the IMU integration error will be large. However, this problem is not significant by using wheel odometry system, due to its nature of generating measurements by counting the wheel rotating impulse.

However, the majority of existing work that use wheel odometry for localization focus on ‘planar surface’ applications, which are typically true *only* for indoor environments [6] [21] [23]. While there are a couple of approaches for performing 6D localization using wheel odometry measurements, the proposed information utilization approaches appear to be *sub-optimal*. Those methods either approximate motion model or wheel odometry measurements at a cost of accuracy reduction [24], or rely on other sensors, e.g., an IMU [25]. The latter type of methods typically requires downgrading (by sub-sampling or partially removing) the usage of wheel odometry measurements, which will also lead to information loss and eventually accuracy loss. To the best of authors’ knowledge, the problem of fully probabilistically using wheel odometry measurements for high-precision 6D localization remains unsolved.

To this end, in this paper, we propose a novel probabilistic framework that is able to use measurements from both a monocular camera and wheel odometry for high-precision 6D pose estimation. Our key contributions are as follows. Firstly, we propose novel parametric representation for motion manifold on which the ground robot moves. Secondly, we design a method for performing manifold based 6D pose integration with wheel odometry measurements in closed form, without non-probabilistic approximation and information reduction. In addition, we analyze the localization errors caused by manifold representation and present an approach for re-parameterizing manifold equations periodically for error reduction. Moreover, we propose a complete localization algorithm based on a manifold-assisted sliding-window estimator, iteratively fusing measurements from both wheel odometry and a monocular

camera. Measurements from an IMU can also be optionally integrated into the proposed algorithm to further improve the accuracy. Finally, by extensive real-world experiments, we show that, the proposed method outperforms other state-of-the-art algorithms, specifically [12] [13] [21] [24], by a significant margin.

## II. RELATED WORK

In this work, we group the related work into two main categories: localization using cameras and localization for ground robots.

### A. Localization using Cameras

In general, there are two families of camera based localization algorithms: the ones rely on cameras only [26] [27] [28] [29] or the ones fuse measurements from both cameras and other sensors [12] [30] [31] [32]. Typically, camera-only localization methods require building a local map incrementally, and computing camera poses by minimizing the errors computed from projecting the local map onto new incoming images. The errors used for optimization can be either under geometrical form [26] [29] or photometric form [27] [28]. On the other hand, cameras can also be used in combination with other types of sensor for localization, and the common choices include IMU [12] [30], GPS [33], and laser range finders [34]. Once other sensors are used for aiding camera based localization, the step of building a local map becomes not necessary since pose to pose prior estimates can be computed with other sensors [12] [30] [34]. Based on that, computationally light-weighted estimators can be formulated by partially or completely marginalizing all visual features to generate stochastic constraints [12] [20].

In terms of estimator design for camera based localization, there are three popular types: filter based methods [35] [12] [20], iterative optimization based methods [32] [28] [36], and finally learning based methods [37] [38]. The filter based methods are typically used in computationally-constrained platforms for achieving real-time pose estimation [35]. To further improve the localization accuracy, recent work [28] [32] introduced iterative optimization based methods to re-linearize states used for computing both residual vectors and Jacobian matrices. By doing this, linearization errors can be reduced and final localization accuracy can be improved. Inspired by recent success in designing deep neural networks for image classification [39], learning based methods for localization are also under active research and development [37] [38], which in general seek to learn scene geometry representation instead of explicit parametric formulation.

### B. Localization For Ground Robots

Localization for ground robot has been under active research for past decades [40] [41] [42] [43] [44]. [40] is one of the well-known method which uses stereo camera for localizing ground robots. For ground robot localization, laser range finders (LRF) are also widely used, since ground robots are

typically able to afford their relative higher power and heavier weight requirements (compared to miniature drones which are only possible to carry cameras.). A number of algorithms were proposed under this category by using different type of LRFs [10] [43] [44], e.g., a 3D LRF [10], a 2D LRF [44], or a self-rotating 2D LRF [43].

Similar to other tasks, learning based methods were also proposed for localizing ground robots. [45] proposed a bi-directional LSTM deep neural network for IMU integration by assuming zero change along  $z$  axis. This method is able to localize ground robots in indoor environments with higher accuracy compared to traditional IMU integration. The related dataset is also provided in [46]. [42] proposed an approach to compute 2 dimensional semantic occupancy grid map directly from front-view RGB images, via variational encoder-decoder neural network. Compared to traditional approach, this method does not need the use of an IMU to compute roll and pitch and project front-view segmentation results onto a plane. Roll and pitch information is calculated implicitly from the network.

In recent years, there are a couple of low-cost localization methods designed for ground robots, by incorporating the usage of wheel odometry measurements [6] [21] [23]. Specifically, Wu et al. [21] proposed to introduce planar-motion constraints to camera-IMU localization system, and also add wheel odometer measurements for stochastic optimization. The proposed method is shown to improve localization performance in *indoor* environments. Similarly, [23] designed a complete framework for visual-odometer SLAM, in which IMU measurements and wheel odometer measurements were used together for pose integration. Additionally, to better utilize wheel odometer measurements, the intrinsic parameters of wheel odometry can also be calibrated online for performance enhancement [6]. However, [6] [21] [23] only focus on robotic navigation on a *single piece of planar surface*. While this is typically true for most indoor environments, applying those algorithms in complicated outdoor 3D environments (e.g., urban streets) is highly risky.

To enable 6D localization for ground robots, [47] proposed to jointly estimate robot poses as well as ground plane parameters. The ground plane is modeled by polynomial parameters, and the estimation is performed by classifying ground region from images and using sparse geometric points within those regions. However, this algorithm is *not* probabilistically formulated, and the estimation accuracy can not be guaranteed. Our previous work [24] went to the similar direction by modeling the manifold parameters, while with an approximate maximum-a-posteriori estimator. Specifically, we modeled the manifold parameters as part of the state vector and used an iterative optimization based sliding-window estimator for localization [24]. However, to perform 6D pose integration, [24] requires using an IMU and approximating wheel odometry integration equations, which will inevitably result in information loss and accuracy reduction. In this paper, we significantly extend the work of [24], by introducing manifold based probabilistic pose integration in closed form, removing the mandatory needs of using an IMU, and formulating manifold re-parameterization equations. We show that, the proposed algorithm achieves significant better performance

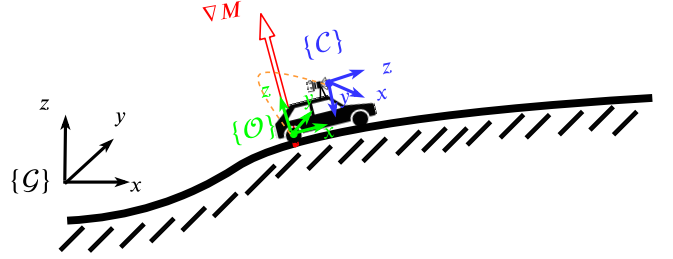


Fig. 2: Conceptual representation of a ground robot moving on a manifold. Global reference frame, sensor reference frames, and the representative direction of the manifold gradient are also shown.

compared to our previous work and other competing state-of-the-art vision based localization methods.

### III. NOTATIONS AND SENSOR MODELS

#### A. Notations

In this work, we assume a ground robot navigating with respect to a global reference frame,  $\{G\}$ , whose wheels are always in contact with the road surface. We use  $\{C\}$  and  $\{O\}$  to denote the camera and the wheel odometry reference frames respectively. The center of frame  $\{O\}$  locates at the center of the robot wheels, with its  $x$ -axis pointing forward and  $z$ -axis pointing up (see Fig. 2 for details). Additionally, we use  ${}^A\mathbf{p}_B$  and  ${}^A_{\mathbf{B}}\bar{\mathbf{q}}$  to represent the position and unit quaternion orientation of frame  $B$  with respect to the frame  $A$ .  ${}^A_{\mathbf{B}}\mathbf{R}$  is the rotation matrix corresponding to  ${}^A_{\mathbf{B}}\bar{\mathbf{q}}$ . We use  $\hat{\mathbf{a}}$ ,  $\bar{\mathbf{a}}$ ,  $\mathbf{a}^T$ ,  $\dot{\mathbf{a}}$ , and  $\|\mathbf{a}\|$  to represent the estimate, error, transpose, time derivative, and 2-norm of the variable  $\mathbf{a}$ . Finally,  $\mathbf{e}_i$  is a  $3 \times 1$  vector, with the  $i$ th element to be 1 and other elements to be 0, and  $\mathbf{e}_{ij} = [\mathbf{e}_i, \mathbf{e}_j]$ .

#### B. Wheel Odometer Measurement Model

Similar to [1], [6], [21], at time  $t$ , the measurements for an intrinsically calibrated wheel odometer system are given by:

$$\mathbf{u}_o(t) = \begin{bmatrix} v_o(t) \\ \omega_o(t) \end{bmatrix} = \begin{bmatrix} \mathbf{e}_1^T \cdot \mathbf{O}^{(t)}\mathbf{v} + n_{v_o} \\ \mathbf{e}_3^T \cdot \mathbf{O}^{(t)}\boldsymbol{\omega} + n_{\omega_o} \end{bmatrix} \quad (1)$$

where  $\mathbf{O}^{(t)}\mathbf{v}$  and  $\mathbf{O}^{(t)}\boldsymbol{\omega}$  are the linear velocity and rotational velocity of the center of frame  $O$  expressed in the frame  $O$  at time  $t$ , and  $n_{v_o}$  and  $n_{\omega_o}$  are measurement noises whose vector forms are  $\mathbf{n}_v = [n_{v_o} \ 0 \ 0]^T$  and  $\mathbf{n}_\omega = [0 \ 0 \ n_{\omega_o}]^T$ . Eq. 1 clearly demonstrates that wheel odometry measurements only provide 2D motion information, i.e., forward linear velocity and rotational velocity about yaw. Therefore, by using measurements only from Eq. 1, it is theoretically possible to conduct planar-surface based pose integration, while infeasible to perform 6D pose integration.

### IV. MANIFOLD BASED 6D POSE INTEGRATION

#### A. Manifold Representation

To allow the usage of the wheel odometry measurements for 6D pose integration, we first model the motion manifold by parametric equations. Specifically, we choose to approximate

the motion manifold around any 3D location  $\mathbf{x}$  by a quadratic polynomial:

$$\mathcal{M}(\mathbf{x}) = z + c + \mathbf{B}^T \begin{bmatrix} x \\ y \end{bmatrix} + \frac{1}{2} \begin{bmatrix} x \\ y \end{bmatrix}^T \mathbf{A} \begin{bmatrix} x \\ y \end{bmatrix} = 0, \mathbf{x} = \begin{bmatrix} x \\ y \\ z \end{bmatrix} \quad (2)$$

with

$$\mathbf{B} = \begin{bmatrix} b_1 \\ b_2 \end{bmatrix}, \mathbf{A} = \begin{bmatrix} a_1 & a_2 \\ a_2 & a_3 \end{bmatrix}. \quad (3)$$

The manifold parameters are:

$$\mathbf{m} = [c \quad b_1 \quad b_2 \quad a_1 \quad a_2 \quad a_3]^\top. \quad (4)$$

We note that traditional methods [1], [6], [21] that assume planar-surface environments are mathematically equivalent to model manifold parameter as  $\mathbf{m} = [c, 0, 0, 0, 0, 0]^\top$ . Their design choices fail to represent the general conditions of outdoor road surface, and thus not suitable for high-precision estimation. To show this statistically, different choices of polynomial representation are also compared in the experiment section (see Sec. VI-B2).

Existing work, e.g., [6], [21], demonstrates difficulties of using odometry measurements for 6D localization. This is primarily due to the fact that odometry only provides 2D measurement (see Eq. 1). By using those measurements only, it is not feasible to perform pose integration in 6D.

However, with manifold representation defined, i.e., Eq. 4, 6D pose integration becomes feasible. To present the details, we first note that:

$$\mathbf{G}_{\mathbf{O}(t)} \dot{\mathbf{R}} = \mathbf{G}_{\mathbf{O}(t)} \mathbf{R} \cdot [\mathbf{O}^{(t)} \boldsymbol{\omega}] \quad (5)$$

where

$$[\boldsymbol{\omega}] = \begin{bmatrix} 0 & -\omega_z & \omega_y \\ \omega_z & 0 & -\omega_x \\ -\omega_y & \omega_x & 0 \end{bmatrix}, \boldsymbol{\omega} = \begin{bmatrix} \omega_x \\ \omega_y \\ \omega_z \end{bmatrix} \quad (6)$$

To perform orientation integration,  $\mathbf{O}^{(t)} \boldsymbol{\omega}$  needs to be known. However, it is clear that the odometry measurement only provides the third element of  $\mathbf{O}^{(t)} \boldsymbol{\omega}$ , as described in Eq. 1. To obtain the first two elements of  $\mathbf{O}^{(t)} \boldsymbol{\omega}$ , information about the manifold representation needs to be used. To derive the equations, we first write:

$$[\mathbf{G}_{\mathbf{O}(t)} \mathbf{R} \cdot \mathbf{e}_3] \cdot \nabla \mathcal{M}(\mathbf{G}_{\mathbf{P}\mathbf{O}(t)}) = \mathbf{0} \quad (7)$$

This equation represents that, the motion manifold  $\mathcal{M}$  has explicitly defined roll and pitch of a ground robot, which should be in consistent with  $\mathbf{G}_{\mathbf{O}(t)} \mathbf{R}$ . In other words, the manifold gradient vector should be in parallel with  $\mathbf{G}_{z\mathbf{O}}$  (see Fig. 2). Taking time derivative of Eq. 7 leads to:

$$[\mathbf{G}_{\mathbf{O}(t)} \dot{\mathbf{R}} \mathbf{e}_3] \nabla \mathcal{M}(\mathbf{G}_{\mathbf{P}\mathbf{O}(t)}) + [\mathbf{G}_{\mathbf{O}(t)} \mathbf{R} \mathbf{e}_3] \nabla \dot{\mathcal{M}}(\mathbf{G}_{\mathbf{P}\mathbf{O}(t)}) = \mathbf{0} \quad (8)$$

By using  $\mathcal{M}(t) = \mathcal{M}(\mathbf{G}_{\mathbf{P}\mathbf{O}(t)})$  for abbreviation, and substituting Eq. 7 into Eq. 8, we obtain:

$$[\mathbf{G}_{\mathbf{O}(t)} \mathbf{R} [\mathbf{O}^{(t)} \boldsymbol{\omega}] \mathbf{e}_3] \nabla \mathcal{M}(t) + [\mathbf{G}_{\mathbf{O}(t)} \mathbf{R} \cdot \mathbf{e}_3] \nabla \dot{\mathcal{M}}(t) = \mathbf{0} \quad (9)$$

$$\Rightarrow [\mathbf{G}_{\mathbf{O}(t)} \mathbf{R}^T \nabla \mathcal{M}(t)] [\mathbf{O}^{(t)} \boldsymbol{\omega}] \mathbf{e}_3 + [\mathbf{G}_{\mathbf{O}(t)} \mathbf{R}^T \nabla \dot{\mathcal{M}}(t)] \mathbf{e}_3 = \mathbf{0} \quad (10)$$

$$\Rightarrow [\mathbf{G}_{\mathbf{O}(t)} \mathbf{R}^T \nabla \mathcal{M}(t)] [\mathbf{e}_3] \mathbf{O}^{(t)} \boldsymbol{\omega} = [\mathbf{G}_{\mathbf{O}(t)} \mathbf{R}^T \nabla \dot{\mathcal{M}}(t)] \mathbf{e}_3 \quad (11)$$

From the above equation, the first two elements in  $\mathbf{O}^{(t)} \boldsymbol{\omega}$  can be calculated, while the third element cannot be identified since  $\mathbf{O}^{(t)} \boldsymbol{\omega}$  is left multiplied by  $[\mathbf{e}_3]$ :

$$[\mathbf{e}_3] = \begin{bmatrix} \mathbf{\Pi} & \mathbf{0}_{2 \times 1} \\ \mathbf{0}_{1 \times 2} & 0 \end{bmatrix}, \mathbf{\Pi} = \begin{bmatrix} 0 & -1 \\ 1 & 0 \end{bmatrix} \quad (12)$$

On the other hand, the third element in  $\mathbf{O}^{(t)} \boldsymbol{\omega}$  can be directly available from the wheel odometry measurement (see Eq. 1). Those observations verify our design motivation of combining wheel odometry measurement and manifold representation together, to rely on their complementary properties for performing 6D pose integration.

To complete our derivation, we seek to obtain the first and second elements of  $\mathbf{O}^{(t)} \boldsymbol{\omega}$  from Eq. 11. To do this, we first write the following equation based on Eq. 7:

$$\nabla \mathcal{M}(t) = \|\nabla \mathcal{M}(t)\| \cdot \mathbf{G}_{\mathbf{O}(t)} \mathbf{R} \cdot \mathbf{e}_3 \quad (13)$$

As a result, Eq. 11 becomes:

$$\|\nabla \mathcal{M}(t)\| [\mathbf{e}_3] [\mathbf{e}_3] \mathbf{O}^{(t)} \boldsymbol{\omega} = [(\mathbf{G}_{\mathbf{O}(t)} \mathbf{R}^T \cdot \nabla \dot{\mathcal{M}}(t))] \mathbf{e}_3 \quad (14)$$

$$\Rightarrow \|\nabla \mathcal{M}(t)\| \mathbf{O}^{(t)} \boldsymbol{\omega}_{12} = \mathbf{e}_{12}^T [\mathbf{e}_3] (\mathbf{G}_{\mathbf{O}(t)} \mathbf{R}^T \cdot \nabla \dot{\mathcal{M}}(t)) \quad (15)$$

$$\Rightarrow \mathbf{O}^{(t)} \boldsymbol{\omega}_{12} = \frac{1}{\|\nabla \mathcal{M}(t)\|} \mathbf{e}_{12}^T [\mathbf{e}_3] (\mathbf{G}_{\mathbf{O}(t)} \mathbf{R}^T \cdot \nabla \dot{\mathcal{M}}(t)) \quad (16)$$

where  $\mathbf{O}^{(t)} \boldsymbol{\omega}_{12} = \mathbf{e}_{12}^T \mathbf{O}^{(t)} \boldsymbol{\omega}$ . We note that, in Eq. 14, we have used the equality:

$$[\mathbf{e}_3] [\mathbf{e}_3] = \begin{bmatrix} \mathbf{\Pi} & \mathbf{0} \\ \mathbf{0} & 0 \end{bmatrix} \begin{bmatrix} \mathbf{\Pi} & \mathbf{0} \\ \mathbf{0} & 0 \end{bmatrix} = - \begin{bmatrix} \mathbf{I}_2 & \mathbf{0} \\ \mathbf{0} & 0 \end{bmatrix} \quad (17)$$

By considering odometry measurements, we have:

$$\mathbf{O}^{(t)} \boldsymbol{\omega} = \begin{bmatrix} \frac{1}{\|\nabla \mathcal{M}(t)\|} \mathbf{e}_{12}^T [\mathbf{e}_3] (\mathbf{G}_{\mathbf{O}(t)} \mathbf{R}^T \cdot \nabla \dot{\mathcal{M}}(t)) \\ \omega_o(t) - n_{\omega_o} \end{bmatrix} \quad (18)$$

By integrating Eq. 18, 3D rotation estimates can be computed. Once rotation is computed, we compute position by integrating:

$$\mathbf{G}_{\dot{\mathbf{P}}\mathbf{O}(t)} = \mathbf{G}_{\mathbf{v}\mathbf{O}(t)} = \mathbf{G}_{\mathbf{O}(t)} \mathbf{R} \cdot \mathbf{O}^{(t)} \mathbf{v} = \mathbf{G}_{\mathbf{O}(t)} \mathbf{R} \begin{bmatrix} v_o - n_{v_o} \\ 0 \\ 0 \end{bmatrix} \quad (19)$$

We also note that our manifold representation, i.e., Eq. 2, implicitly defines a motion model that the integrated position must satisfy,  $\mathcal{M}(\mathbf{G}_{\mathbf{P}\mathbf{O}(t)}) = 0$ . Actually, the representation of

Eq. 19 exactly follows the manifold constraint. To show the details, we note that:

$$\begin{aligned} \mathcal{M}(\mathbf{G}_{\mathbf{p}_{\mathbf{O}(t)}}) = 0 &\Rightarrow \frac{\partial \mathcal{M}(\mathbf{G}_{\mathbf{p}_{\mathbf{O}(t)}})}{\partial t} = 0 & (20) \\ \Rightarrow \nabla \mathcal{M}(\mathbf{G}_{\mathbf{p}_{\mathbf{O}(t)}})^T \cdot \mathbf{G}_{\mathbf{v}_{\mathbf{O}(t)}} = 0 &\Rightarrow \mathbf{e}_3^T \cdot \mathbf{G}_{\mathbf{O}(t)} \mathbf{R} \cdot \mathbf{G}_{\mathbf{v}_{\mathbf{O}(t)}} = 0 & (21) \end{aligned}$$

where  $\mathbf{G}_{\mathbf{O}(t)} \mathbf{R}^T \mathbf{e}_3$  is proportional to  $\nabla \mathcal{M}(\mathbf{G}_{\mathbf{p}_{\mathbf{O}(t)}})$  in Eq. 21. The expression of  $\mathbf{G}_{\mathbf{v}_{\mathbf{O}(t)}}$  in Eq. 19 clearly satisfies the manifold constraint defined in Eq. 21.

With Eq. 18 and 19 being defined, we are able to perform odometry based 6D pose integration on a manifold. The entire process does not include using of an IMU. To intuitively explain the process, we note that, performing 6D pose integration requires resolving 6 degrees-of-freedom using either sensor's measurements or motion constraints. In our system, 2 degrees-of-freedom are provided by wheel odometry measurements (see Eq. 1), 2 degrees-of-freedom are from the non-holonomic motion constraint<sup>3</sup>, and the last 2 degrees-of-freedom are determined by the manifold equation (i.e., first two elements in Eq. 18). The intuitive explanation exactly meets our mathematical derivations.

### B. State and Error-State Prediction

In this section, we describe the details of using the proposed manifold representation for performing state and error-state propagation, which is a necessary prerequisite for formulating probabilistic estimators [48]. Since the integration process requires explicit representation of both poses (position and orientation vectors) and manifold equations, we define the state vector as follows:

$$\mathbf{x} = [\mathbf{G}_{\mathbf{p}_{\mathbf{O}}}^T \quad \mathbf{G}_{\mathbf{q}}^T \quad \mathbf{m}^T]^T \quad (22)$$

The time evolution of the state vector can be described by:

$$\mathbf{G}_{\dot{\mathbf{p}}_{\mathbf{O}(t)}} = \mathbf{G}_{\mathbf{O}(t)} \mathbf{R}^{\mathbf{O}(t)} \mathbf{v} \quad (23)$$

$$\mathbf{G}_{\mathbf{O}(t)} \dot{\mathbf{q}} = \frac{1}{2} \mathbf{G}_{\mathbf{O}(t)} \mathbf{q} \cdot \boldsymbol{\Omega}(\mathbf{O}(t) \boldsymbol{\omega}) \quad (24)$$

$$\dot{\mathbf{m}}(t) = \mathbf{0} \quad (25)$$

where

$$\boldsymbol{\Omega}(\boldsymbol{\omega}) = \begin{bmatrix} -[\boldsymbol{\omega}] & \boldsymbol{\omega} \\ -\boldsymbol{\omega}^T & 0 \end{bmatrix} \quad (26)$$

We point out that the motion dynamics of the manifold parameters will be specifically described later in Sec. IV-C, and we here ignore the discussion on Eq. 25. Based on the above equations, the dynamics of the estimated poses can be written as:

$$\mathbf{G}_{\hat{\mathbf{p}}_{\mathbf{O}(t)}} = \mathbf{G}_{\mathbf{O}(t)} \hat{\mathbf{R}} [v_o(t) \quad 0 \quad 0]^T \quad (27)$$

$$\mathbf{G}_{\mathbf{O}(t)} \hat{\mathbf{q}} = \frac{1}{2} \mathbf{G}_{\mathbf{O}(t)} \hat{\mathbf{q}} \cdot \boldsymbol{\Omega}(\mathbf{O}(t) \hat{\boldsymbol{\omega}}) \quad (28)$$

$$\dot{\mathbf{m}}(t) = \mathbf{0} \quad (29)$$

<sup>3</sup>This is implicitly introduced in Eq. 19, in which local velocity only contains non-zero values along x-axis. Robots equipped with mecanum wheels are not under this constraint, and the equations must be re-designed. However, this type of wheels is not commonly used in commercial outdoor robots and vehicles.

where

$$\mathbf{O}(t) \hat{\boldsymbol{\omega}} = \begin{bmatrix} \frac{1}{\|\nabla \hat{\mathcal{M}}(t)\|} \mathbf{e}_{12}^T [\mathbf{e}_3] (\mathbf{G}_{\mathbf{O}(t)} \hat{\mathbf{R}}^T \cdot \nabla \hat{\mathcal{M}}(t)) \\ \boldsymbol{\omega}_o(t) \end{bmatrix} \quad (30)$$

Eqs. 27 to 29 can be integrated with wheel odometry measurement via numerical integration methods (e.g., Runge-Kutta).

To describe the details of error-state propagation, we first employ first-order approximation of Taylor series expansion on Eq. 18, to obtain:

$$\mathbf{O}(t) \boldsymbol{\omega} = \mathbf{O}(t) \hat{\boldsymbol{\omega}} + \mathbf{O}(t) \tilde{\boldsymbol{\omega}} = \mathbf{O}(t) \hat{\boldsymbol{\omega}} + \mathbf{J}_x \tilde{\mathbf{x}} + \mathbf{J}_n \mathbf{n} \quad (31)$$

where

$$\mathbf{n} = [n_{v_o} \quad n_{\omega_o}]^T \quad (32)$$

and

$$\mathbf{J}_x = \frac{\partial \mathbf{O}(t) \boldsymbol{\omega}}{\partial \mathbf{x}}, \quad \mathbf{J}_n = \frac{\partial \mathbf{O}(t) \boldsymbol{\omega}}{\partial \mathbf{n}} \quad (33)$$

By defining local orientation error  $\delta \boldsymbol{\theta}$  [48]:

$$\mathbf{G}_{\mathbf{R}} \simeq (\mathbf{I} - [\delta \boldsymbol{\theta}]) \mathbf{G}_{\hat{\mathbf{R}}} \quad (34)$$

we are able to write:

$$\dot{\delta \boldsymbol{\theta}} = -[\mathbf{O}(t) \hat{\boldsymbol{\omega}}] \delta \boldsymbol{\theta} + \mathbf{J}_x \tilde{\mathbf{x}} + \mathbf{J}_n \mathbf{n} \quad (35)$$

The detailed derivation of Eq. 35 is shown in Appendix A-B. Since  $\delta \boldsymbol{\theta}$  is part of  $\tilde{\mathbf{x}}$ , first two terms in Eq. 35 can be combined for formulating:

$$\dot{\delta \boldsymbol{\theta}} = \bar{\mathbf{J}}_x \tilde{\mathbf{x}} + \mathbf{J}_n \mathbf{n} \quad (36)$$

In terms of position, based on Eq. 19, it is straightforward to obtain:

$$\mathbf{G}_{\dot{\mathbf{p}}_{\mathbf{O}(t)}} = \mathbf{G}_{\mathbf{O}(t)} \hat{\mathbf{R}} (\mathbf{I} + [\delta \boldsymbol{\theta}]) \begin{bmatrix} v_o - n_{v_o} \\ 0 \\ 0 \end{bmatrix} - \mathbf{G}_{\mathbf{O}(t)} \hat{\mathbf{R}} \begin{bmatrix} v_o \\ 0 \\ 0 \end{bmatrix} \quad (37)$$

$$= -\mathbf{G}_{\mathbf{O}(t)} \hat{\mathbf{R}} \begin{bmatrix} v_o \\ 0 \\ 0 \end{bmatrix} \delta \boldsymbol{\theta} - \mathbf{G}_{\mathbf{O}(t)} \hat{\mathbf{R}} \begin{bmatrix} n_{v_o} \\ 0 \\ 0 \end{bmatrix} \quad (38)$$

For the manifold parameters we have:

$$\dot{\mathbf{m}} = \mathbf{0} \quad (39)$$

With Eqs. 35, 38, 39 being defined, we are able to perform error-state integration in 6D. To put all equations in the vector form, we have the error state equation as:

$$\dot{\tilde{\mathbf{x}}} = \mathbf{F}_c \cdot \tilde{\mathbf{x}} + \mathbf{G}_c \cdot \mathbf{n}, \quad \tilde{\mathbf{x}} = [\delta \boldsymbol{\theta}^T \quad \mathbf{G}_{\hat{\mathbf{p}}_{\mathbf{O}}}^T \quad \tilde{\mathbf{m}}^T]^T \quad (40)$$

where

$$\mathbf{F}_c = \begin{bmatrix} \mathbf{0}_{3 \times 3} & -\mathbf{G}_{\hat{\mathbf{R}}} [\mathbf{O} \mathbf{v}] & \mathbf{0}_{3 \times 6} \\ \mathbf{0}_{3 \times 3} & -[\mathbf{O} \hat{\boldsymbol{\omega}}] & \mathbf{0}_{3 \times 6} \\ \mathbf{0}_{6 \times 3} & \mathbf{0}_{6 \times 3} & \mathbf{0}_{6 \times 6} \end{bmatrix} + \begin{bmatrix} \mathbf{0}_{3 \times 12} \\ \mathbf{J}_x \\ \mathbf{0}_{6 \times 12} \end{bmatrix} \quad (41)$$

and

$$\mathbf{G}_c = \begin{bmatrix} -(\mathbf{G}_{\hat{\mathbf{R}}})_{[:,1]} & \mathbf{0}_{3 \times 1} \\ (\mathbf{J}_n)_{[:,1]} & (\mathbf{J}_n)_{[:,2]} \\ \mathbf{0}_{6 \times 1} & \mathbf{0}_{6 \times 1} \end{bmatrix} \quad (42)$$

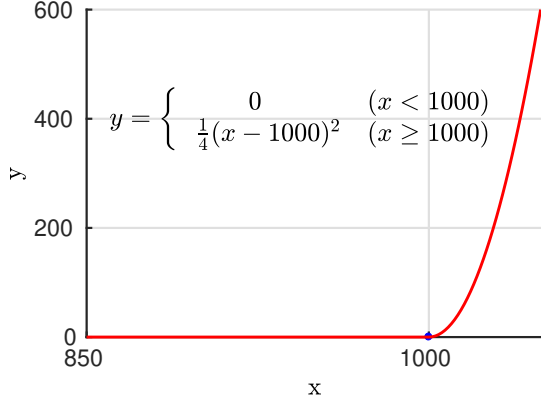


Fig. 3: Example two-dimensional manifold, concatenated by a zeroth-order and a second-order polynomial equation.

with  $(\cdot)_{[i,j]}$  representing the  $i$ th column of a matrix. We note that  $\mathbf{F}_c$  and  $\mathbf{G}_c$  are continuous-time error-state transition matrix and noise Jacobian matrix. To implement a discrete-time probabilistic estimator, discrete-time error state transition matrix  $\Phi(t, \tau)$  is required. This can be achieved by integrating

$$\dot{\Phi}(t, \tau) = \mathbf{F}_c(t)\Phi(t, \tau), \quad \Phi(\tau, \tau) = \mathbf{I}_{12 \times 12} \quad (43)$$

using numerical integration methods. The detailed implementation of numerical integration and the remaining steps are standard ones for discrete-time localization estimators, which can be found at [12], [48].

### C. Manifold Re-Parameterization

Eq. 2 defines a motion manifold in global reference frame, which is mathematically correct and able to formulate a stochastic estimator easily. However, this representation makes the propagation process of the manifold parameter  $\mathbf{m}$  extremely challenging. Specifically, it is difficult to characterize the motion dynamics of the manifold, which changes over time. [24] simply uses  $\dot{\mathbf{m}} = \mathbf{n}_{\omega m}$ , with  $\mathbf{n}_{\omega m}$  being a zero-mean Gaussian noise vector. However, this method has limitations for large-scale deployment.

To illustrate the details, let's look at the following equation as an example trajectory:

$$y = \begin{cases} 0 & x < 1000 \\ \frac{1}{4}(x - 1000)^2 & x \geq 1000 \end{cases} \quad (44)$$

This equation is also plotted in Fig. 3. In fact, Eq. 44 can be considered as a two-dimensional manifold. If a *quadratic* two-dimensional manifold is represented in general by:

$$y + c + bx + ax^2 = 0 \quad (45)$$

Eq. 44 is in fact a piece-wise quadratic two-dimensional manifold, whose parameters in piece-wise form are:

$$\begin{cases} c=0, b=0, a=0 & x < 1000 \\ c=2.5 \cdot 10^5, b=-500, a=0.25 & x \geq 1000 \end{cases} \quad (46)$$

Clearly, there will be a 'significant' jump in the estimate of manifold parameters at  $x = 1000$ , due to our choice of quadratic representation to model a non-quadratic equation.

If we were able to use infinite number of polynomials for manifold approximation, this problem should not have been caused. However, this is computationally not feasible. As a result, normal propagation process for manifold parameters (see Eq. 25) cannot capture this type of changes. Although the manifold representation is still feasible under this condition, by removing and re-initializing the manifold parameters, this is definitely not *preferred* for high-precision pose estimation.

To this end, we propose to modify Eq. 45 as:

$$y + c_{new} + b_{new}(x - x_o) + a_{new}(x - x_o)^2 = 0 \quad (47)$$

where  $x_o$  is a fixed constant parameter, which can be obtained by the current estimate of  $x$ . If when  $x = 1000$ , we obtain an estimate  $x_o = 999.9$ , instead of the 'significant jump' in Eq. 46 we have:

$$c_{new} = 0.0025, \quad b_{new} = 0.05, \quad a_{new} = 0.25, \\ \text{when } x=1000, \text{ with } x_o = 999.9 \quad (48)$$

By using  $x_o$ , the 'jump' for the manifold parameters is largely reduced. This make the manifold propagation equations (in terms of both state estimate and error-state estimate) feasible.

By illustrating our motivation and high-level concept with the above example, we introduce our formal mathematical equation of the 'local' manifold representation and re-parameterization. By assuming the previous re-parameterization step is performed at time  $t_k$  and the next one is triggered at  $t_{k+1}$ , we have

$$\mathbf{m}(t_{k+1}) = \underbrace{\begin{bmatrix} 1 & \delta \mathbf{x}^T & \gamma^T \\ \mathbf{0} & \delta \mathbf{R}^T & \Xi \\ \mathbf{0} & \mathbf{0} & \Psi \end{bmatrix}}_{\Lambda(t_k)} \mathbf{m}(t_k), \quad \text{with} \quad \begin{cases} \delta \mathbf{R} = \mathbf{R}_o \mathbf{R}_1^{-1} \\ \delta \mathbf{x} = \mathbf{R}_o(\mathbf{x}_1 - \mathbf{x}_o) \end{cases} \quad (49)$$

In Eq. 49,  $\mathbf{R}_o$  and  $\mathbf{x}_o$  are the *fixed* re-parameterization parameters for  $\mathbf{m}(t_k)$ , and  $\mathbf{R}_1$  and  $\mathbf{x}_1$  are those for  $\mathbf{m}(t_{k+1})$ .  $\gamma$ ,  $\Xi$ , and  $\Psi$  are all functions of  $\delta \mathbf{R}$  and  $\delta \mathbf{x}$ . For choosing the re-parameterization parameters, similarly to Eq. 48, we choose the *first* estimate of  ${}^G \mathbf{p}_{\mathbf{O}(t_k)}$  for  $\mathbf{x}_o$  and that of  ${}^G \mathbf{p}_{\mathbf{O}(t_{k+1})}$  for  $\mathbf{x}_1$ . The detailed derivation of 49 and parameter choices of  $\mathbf{R}_o$  and  $\mathbf{R}_1$  can be found in Appendix C.

Therefore, by employing Eq. 49, we are able to re-parameterize manifold representation around any time  $t$ , for both state estimates and their corresponding uncertainties. We note that this is similar to re-parameterize SLAM features with inverse depth parameterization [35], [15]. It is important to point out that, during our re-parameterization process,  $\mathbf{R}_o$ ,  $\mathbf{x}_o$ ,  $\mathbf{R}_1$ ,  $\mathbf{x}_1$  are used as a *fixed* constant vectors and matrices, in stead of *random variables*. This removes the needs of computing the corresponding Jacobians with respect to them, which is also a widely used skill in SLAM feature re-parameterization [35], [15].

We also point out that, our mathematical derivation and representation in previous sections are all based on using  $\mathbf{m}$  (in Sec. IV-A - IV-B and Appendix B), which is before any re-parameterization step. Once re-parameterization is introduced, the manifold stored in the state vector at time  $t_{k+1}$  becomes

$\mathbf{m}(t_{k+1})$  while the corresponding manifold parameters used in state integration remains  $\mathbf{m}$ . This is due to the fact that global manifold representation keeps unchanged. The relation between  $\mathbf{m}$  and  $\mathbf{m}(t_{k+1})$  is:

$$\mathbf{m}(t_{k+1}) = \mathbf{\Lambda}(t_k)\mathbf{m}(t_k) \quad (50)$$

$$= \mathbf{\Lambda}(t_k)\mathbf{\Lambda}(t_{k-1})\mathbf{m}(t_{k-1}) = \cdots = \prod_{i=0}^k \mathbf{\Lambda}(t_i)\mathbf{m} \quad (51)$$

Thus, during state prediction and Jacobian computation, we can simply apply  $\mathbf{m} = (\prod_{i=0}^k \mathbf{\Lambda}(t_i))^{-1}\mathbf{m}(t_k)$ . This allows explicitly considering the uncertainties in  $\mathbf{m}(t_{k+1})$  without incurring additional computational cost and complex software design.

With the manifold re-parameterization process defined, we revisit the problem of characterizing the motion dynamics of the motion manifold. Since the actual manifold on which a ground robot navigates changes over time, this fact must be explicitly modeled for accuracy guarantees. Specifically, we propose to take this into account during the re-parameterization process as:

$$\mathbf{m}(t_{k+1}) = \mathbf{\Lambda}(t_k)\mathbf{m}(t_k) + \mathbf{n}_{wm} \quad (52)$$

$$\mathbf{e}_i^T \mathbf{n}_{wm} \sim \mathcal{N}(0, \sigma_{i,wm}^2) \text{ with } i = 1, \dots, 6 \quad (53)$$

where  $\mathcal{N}(0, \sigma_{i,wm}^2)$  represents Gaussian distribution with mean 0 and variance  $\sigma_{i,wm}^2$ . Specifically,  $\sigma_{i,wm}$  is defined by:

$$\sigma_{i,wm} = \alpha_{i,p} \|\delta \mathbf{x}\| + \alpha_{i,q} \|\delta \mathbf{R}\| \quad (54)$$

It is important to point out in our proposed formulation, the manifold uncertainties (i.e.,  $\sigma_{i,wm}$ ) are functions of spatial displacement (see Eq. 54). This is different from standard noise propagation equations in VIO literatures [12], [30], in which noises are characterized by functions of time. Since the motion manifold is a ‘spatial’ concept instead of a ‘temporal’ concept, our design choice better fits our localization problem.

## V. LOCALIZATION ALGORITHM

To allow high-precision localization for ground robots, in this section, we propose a detailed localization algorithm for fusing measurements from a monocular camera, wheel odometry, and optionally an IMU. Specifically, we present a sliding-window iterative optimization based algorithms for minimizing the cost functions derived from both sensor measurements and manifold constraints. In what follows, we first describe our proposed method without using an IMU, and the extra operations related to IMU will be discussed in Sec. V-E.

### A. Data Interpolation

In this paper, we assume that, the wheel odometry and camera sensors are perfectly synchronized by hardware, and the camera is rigidly connected to the robot. Before presenting the details of probabilistic sensor fusion, we first note that data interpolation is required in our system. This is due to the fact that a couple of operations in the proposed system require performing odometry based pose integration between images (e.g., the operation in Sec. V-B). However, due to

---

### Algorithm 1 Proposed Localization Algorithm.

---

**Propagation:** Propagate state vector using odometry readings as well as current estimated manifold parameters (Sec. IV-B).

**Update:** when a new image is recorded and the condition of allocating a new keyframe is satisfied,

- 1: Image Processing: Performing feature extraction, matching, and geometrical verification (Sec. V-B).
  - 2: Iterative Optimization: Performing statistical optimization using cost functions of odometry propagation, camera observations, prior term, manifold constraint (Eq. 55 in Sec. V-C). IMU integration term can also be added optionally (Eq. 65 in Sec. V-E).
  - 3: State Marginalization: Marginalizing estimated features, oldest keyframes, and pose integration constraints (Eq. 60-61 in Sec. V-C). If an IMU is used, we also marginalize IMU velocities and biases that are not corresponding to the latest keyframe (Sec. V-E).
  - 4: Manifold Re-Parameterization: Parameterizing motion manifold using the estimated position of the latest keyframe and also performing uncertainty propagation (Sec. IV-C).
- 

the nature of the multi-sensor system, we might not have wheel odometer measurements at exactly the same time when images are captured. To this end, we propose to compute extra ‘virtual’ wheel odometer measurements by interpolating the closest measurements before and after the image’s timestamp. Since the wheel odometer measurements are at relatively high frequencies (e.g.,  $\geq 100\text{Hz}$  in our case) and ground robots in human-made environments are typical under smoothed motion, we choose to apply linear interpolation.

### B. Image Processing

Once a new image is received, we proceed to perform pose integration to compute the corresponding predicted pose by wheel odometer measurements and manifold representation (see Sec. V-D). Once enough translational or rotational displacement is detected by pose prediction (e.g., 20 centimeters and 3 degrees in our tests), the new image will be processed, otherwise it will be dropped. For feature processing, FAST features [49] are extracted and FREAK [50] descriptors are computed due to their efficiency on low-cost processors, which is followed by feature matching and RANSAC geometrical verification steps.

### C. State Vector and Iterative Optimization

To illustrate the localization algorithm, we first introduce the state vector. At timestamp  $t_k$ , the state vector is <sup>4</sup>:

$$\mathbf{y}_k = [\mathbf{O}_k^T \quad \mathbf{x}_k^T]^T, \quad (55)$$

<sup>4</sup>For simpler representation, we ignore sensor extrinsic parameters in our presentation in this section. However, in some of our real world experiments when offline sensor extrinsic calibration is not of high accuracy, those parameters are explicitly modeled in our formulation and used in optimization.

where  $\mathbf{x}$  is defined in Eq. 22 and  $\mathbf{O}_k$  is the sliding-window pose at timestamp  $k$ :

$$\mathbf{O}_k = [\mathbf{x}_{\mathbf{O}_{k-N+1}}^T \cdots \mathbf{x}_{\mathbf{O}_{k-1}}^T]^T, \mathbf{x}_{\mathbf{O}_i} = [\mathbf{G}_{\mathbf{p}_{\mathbf{O}_i}}^T \quad \mathbf{G}_{\mathbf{O}_i} \bar{\mathbf{q}}^T]^T \quad (56)$$

for  $i = k - N + 1, \dots, k - 1$ .

When a new image at  $t_{k+1}$  is recorded, pose integration is performed to compute  $\mathbf{x}_{\mathbf{O}_{k+1}}$  (see Sec. IV-B). Subsequently, we employ the following cost function to refine our state:

$$\begin{aligned} \mathcal{C}_{k+1}(\mathbf{y}_k, \mathbf{x}_{\mathbf{O}_{k+1}}, \mathbf{f}_{k+1}) &= 2 \boldsymbol{\eta}_k^T (\mathbf{y}_k - \hat{\mathbf{y}}_k) + \|\mathbf{y}_k - \hat{\mathbf{y}}_k\|_{\Sigma_k} \\ &+ \sum_{i,j \in \mathbf{S}_{i,j}} \gamma_{i,j} + \sum_{i=k-N+1}^{k+1} \psi_i + \beta_i(\mathbf{x}_k, \mathbf{x}_{k+1}) \end{aligned} \quad (57)$$

where  $\boldsymbol{\eta}_k$  and  $\Sigma_k$  are estimated prior information vector and matrix from the previous timestamp respectively,  $\|\mathbf{a}\|_{\Sigma}$  is computed by  $\mathbf{a}^T \Sigma \mathbf{a}$ ,  $\mathbf{f}_{k+1}$  is the set of visual landmarks involved in the optimization process,  $\mathbf{S}_{i,j}$  represents the set of pairs between keyframes and observed features, and  $\gamma_{i,j}$  is the computed camera reprojection residual vector. Additionally,  $\psi_i$  is the residual corresponding to the motion manifold, and  $\beta_i$  to the pose prediction cost by odometer measurements between time  $t_k$  and  $t_{k+1}$ , described in Sec. IV-B. Specifically, the camera cost function is:

$$\gamma_{i,j} = \sum_{i,j \in \mathbf{S}_{i,j}} \|\mathbf{z}_{ij} - h(\mathbf{x}_{\mathbf{O}_i}, \mathbf{f}_j)\|_{\Sigma_C} \quad (58)$$

where  $\mathbf{z}_{ij}$  represents camera measurement corresponding to the pose  $i$  and visual landmark  $\mathbf{f}_j$ ,  $\Sigma_C$  is the measurement information matrix, and the function  $h(\cdot)$  is the model of a calibrated perspective camera [20].

To model  $h(\cdot)$ ,  $\mathbf{f}_j$  is required. Recent state-of-the-art localization algorithms can choose to estimate  $\mathbf{f}_j$  online [13] or not model it in the state vector [12], or a hybrid method between them [15]. In this work, we choose to not model  $\mathbf{f}_j$  in our state vector (see Eq. 55), similar to [12]. To achieve that, during optimization process, we first compute features' positions via Gauss-Newton based multi-view triangulation method, which are used as initial values in minimizing  $\mathcal{C}_{k+1}$ . We note that, to avoid using the same information multiple times, at each timestamp, we choose *un-processed* features only [21]. With computed positions of features, all prerequisites of solving  $\mathcal{C}_{k+1}$  are prepared.

At each timestamp, we use iterative nonlinear optimization to solve  $\mathcal{C}_{k+1}$ , for obtaining posterior estimates  $\hat{\mathbf{y}}_{k+1}^*$  and  $\hat{\mathbf{f}}_{k+1}^*$ . To keep the computational cost constrained, after the optimization process, we marginalize oldest pose and features  $\mathbf{f}_{k+1}$ . We also marginalize the wheel odometer measurements between poses at  $t_k$  and  $t_{k+1}$ . This process computes new prior terms  $\boldsymbol{\eta}_{k+1}$  and  $\Sigma_{k+1}$ . We here denote the gradient and Hessian matrix of  $\mathcal{C}_k$  with respect to  $[\mathbf{y}_k^T, \mathbf{x}_{\mathbf{O}_{k+1}}^T, \mathbf{f}_{k+1}^T]^T$  as  $\boldsymbol{\psi}$  and  $\Omega$ :

$$\boldsymbol{\psi} = \begin{bmatrix} \psi_r \\ \psi_m \end{bmatrix}, \Omega = \begin{bmatrix} \Omega_{rr} & \Omega_{mr}^T \\ \Omega_{mr} & \Omega_{mm} \end{bmatrix} \quad (59)$$

where  $\psi_m$  and  $\Omega_{mm}$  are corresponding to the terms that are going to be marginalized, e.g., oldest pose and features,  $\psi_r$ ,

and  $\Omega_{rr}$  to the terms to be kept, and  $\Omega_{mr}$  is the cross term. Similarly to other marginalization methods [13], we compute:

$$\boldsymbol{\eta}_{k+1} = \boldsymbol{\psi}_r - \Omega_{mr}^T \Omega_{mm}^{-1} \boldsymbol{\psi}_m \quad (60)$$

$$\Sigma_{k+1} = \Omega_{rr} - \Omega_{mr}^T \Omega_{mm}^{-1} \Omega_{mr} \quad (61)$$

#### D. Manifold Operations

In our proposed optimization algorithm, in addition to the manifold propagation cost  $\beta$ , we also introduce additional cost function  $\boldsymbol{\psi}$  (see Eq. 57), which provides explicitly kinematic constraints for multiple poses in the sliding window based on the motion manifold.

Specifically, if a local motion manifold is perfectly parametrically characterized at around  $\mathbf{G}_{\mathbf{p}_{\mathbf{O}_k}}$ , for any keyframe index  $i$ , the following equation holds:

$$\mathcal{M}(\mathbf{G}_{\mathbf{p}_{\mathbf{O}_k}}) = 0, \text{ if } \|\mathbf{G}_{\mathbf{p}_{\mathbf{O}_k}} - \mathbf{G}_{\mathbf{p}_{\mathbf{O}_i}}\| < \epsilon \quad (62)$$

where  $\epsilon$  is a distance constraint, representing the region size that the local manifold spans. Since modeling errors are inevitable for manifold representation, we model Eq. 62 as a stochastic constraint, similarly to the concept used in [21]. Specifically, we define the residuals of  $\boldsymbol{\psi}_i$  for any valid keyframe (see Eq. 57) as  $\boldsymbol{\psi}_i = [f_{p_i}, f_{q_i}]^T$ , with

$$f_{p_i} = \frac{1}{\sigma_p^2} (\mathcal{M}(\mathbf{G}_{\mathbf{p}_{\mathbf{O}_i}}))^2 \quad (63)$$

and  $\sigma_p^2$  is the corresponding noise variance. Additionally, we apply an orientation cost as:

$$f_q = \left\| \left[ (\mathbf{G}_{\mathbf{O}_i} \mathbf{R} \cdot \mathbf{e}_3) \times \right]_{12} \cdot \frac{\partial \mathcal{M}}{\partial \mathbf{p}} \Big|_{\mathbf{p}=\mathbf{G}_{\mathbf{p}_{\mathbf{O}_i}}} \right\|_{\Sigma_q} \quad (64)$$

where  $[\mathbf{a} \times]_{12}$  are the first two rows of the cross-product matrix of  $\mathbf{a}$ ,  $\Sigma_q$  is the measurement noise information matrix.

We point out that, the manifold parameters used in propagation can be considered as *implicit* constraints, providing frame-to-frame motion information. On the other hand, Eq. 63-64 can be treated as *explicit* constraints for cost function optimizing. This provides multi-frame constraints for poses in the sliding window, to ensure that those are consistently represented under current manifold equations. We will show later in experiments (see Sec. VI), this leads to noticeable performance gain for ground robots and vehicles operating in structured environments (e.g., university campuses and urban streets).

It is also important to note that, our choice of modeling both  $\beta$  and  $\boldsymbol{\psi}$  is probabilistically valid, since the manifold representation basically provides *kinematic* constraints. If an algorithm seeks to use the same sensor measurements, instead of kinematic constraints, in different cost functions, additional correlation terms must be explicitly modeled (see [51] for an example case). However, this is not required in our design.

Additionally, to allow Eq. 52 to capture the changes of manifold correctly, we apply the method described in Sec. IV-C to re-parametrize the manifold parameters at *each* step after the marginalization process is performed. This will convert both state estimates as well as prior information matrix by augmenting  $\mathbf{m}(t_{k+1})$  into the state vector and marginalizing



$\mathbf{m}(t_k)$ . We will show in experiments that, this is a critical step for improving localization precision. We also note that in Eq. 2 we choose to fix the coefficient of  $z$  to be 1, which means that our manifold representation is *not* generic. However, this perfectly fits our applications, since most ground robots can *not* climb vertical walls.

### E. Localization by adding an IMU

Since IMU is also a widely used low-cost sensor, we also propose algorithmic modifications of the proposed method, to be able to use measurements from an IMU to further improve the localization accuracy.

Specifically, when an IMU is used in combination with wheel odometry and a monocular camera, the state vector of the localization algorithm (see Eq. 55) becomes:

$$\mathbf{y}_k = [\mathbf{O}_k^T \quad \mathbf{x}_k^T \quad \mathbf{u}_k^T]^T, \mathbf{u}_k = [\mathbf{G}\mathbf{v}_{\mathbf{I}_k}^T \quad \mathbf{b}_{\mathbf{a}_k}^T \quad \mathbf{b}_{\mathbf{g}_k}^T]^T \quad (65)$$

where  $\mathbf{G}\mathbf{v}_{\mathbf{I}_k}$  is IMU's velocity expressed in global frame, and  $\mathbf{b}_{\mathbf{a}_k}$  and  $\mathbf{b}_{\mathbf{g}_k}$  are accelerometer and gyroscope biases respectively. Once a new image is received and a new keyframe is determined, we iteratively optimize the IMU-assisted cost function:

$$\begin{aligned} C'_{k+1}(\mathbf{y}_k, \mathbf{x}_{\mathbf{O}_{k+1}}, \mathbf{f}_{k+1}, \mathbf{u}_{k+1}) &= C_{k+1}(\mathbf{y}_k, \mathbf{x}_{\mathbf{O}_{k+1}}, \mathbf{f}_{k+1}) \\ &\quad + \kappa(\mathbf{x}_{\mathbf{O}_k}, \mathbf{x}_k, \mathbf{x}_{\mathbf{O}_{k+1}}, \mathbf{x}_{k+1}) \end{aligned} \quad (66)$$

Compared to Eq. 57 when IMU is not used, Eq. 66 only requires an additional IMU cost  $\kappa(\cdot)$ . Since IMU cost functions are mature and described in a variety of existing literatures [12], [32], [30], we here omit the discussion on detailed formulation of  $\kappa(\cdot)$ . The last modification step that enables using IMU measurements is the state marginalization process, in which  $\mathbf{u}_k$  and the IMU measurements between  $\mathbf{u}_k$  and  $\mathbf{u}_{k+1}$  will also be marginalized. The overall algorithm steps are shown in Alg. 1

### F. Localization with Pre-built Map

The method described in previous sections defines an open-loop localization algorithm, in which long-term drift is inevitable. Since persistent re-localization with pre-built maps for ground robot is required for various robotic tasks, we also implement an algorithm to enable the proposed methods to be used for persistent re-localization.

Our framework of persistent re-localization is similar to that of [14] [31], and we here briefly go over the steps. To be able to use a pre-built map, the position and orientation between the map frame and global frame, i.e.,  $\mathbf{G}\mathbf{p}_M$  and  $\mathbf{G}\mathbf{q}_M$ , need to be modeled into state vector (Eq. 55) and be estimated online. In our persistent re-localization framework, all operations of normal open-loop localization remain the same, with one additional operation added: associate features detected from incoming images to visual 3D landmarks in the map and use that for formulating extra cost functions. This is achieved by combination of appearance based loop closure query and geometrical consistent verification [14]. We will

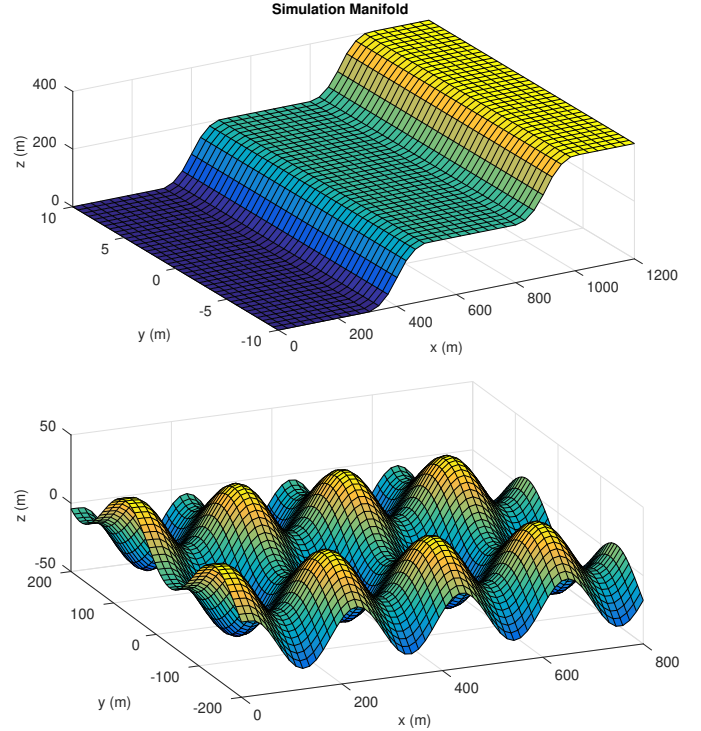


Fig. 4: Motion manifold used in simulation tests. Top: Motion manifold constructed by piece-wise quadratic polynomials. Bottom: Motion manifold constructed by sinusoidal and cosinusoidal functions.

show later in experiment section (Sec. VI-B5), by using our proposed manifold based optimization method, the accuracy of persistent re-localization can also be improved.

## VI. EXPERIMENTS

In this section, we show results from both simulation tests and real-world experiments to demonstrate the performance of the proposed methods.

### A. Simulation Tests

In the simulation tests, we assumed a ground robot moving on a manifold, whose gradient vectors are continuous in  $\mathcal{R}^3$ . Specifically, we generated two types of manifold for simulations, shown in Fig. 4. The first type of motion manifold (top one in Fig. 4) is generated by piece-wise polynomial functions, and the corresponding manifold parameters are plotted in Fig. 6. As discussed in Sec. IV-C, Eq. 2 represents motion manifold in global frame and thus the corresponding parameters can change significantly over space (see Fig. 6). By simulating motion manifold in this setup, the overall performance of the proposed algorithm and the capability of handling changes of motion manifold can be evaluated. The second type (bottom one in Fig. 4) of manifold is generated by planar and sinusoidal functions. This is to simulate the fact that in real-world scenarios, ‘quadratic’ equations are basically ‘local’ approximations which in general cannot perfectly characterize all road conditions. With this simulated environment,

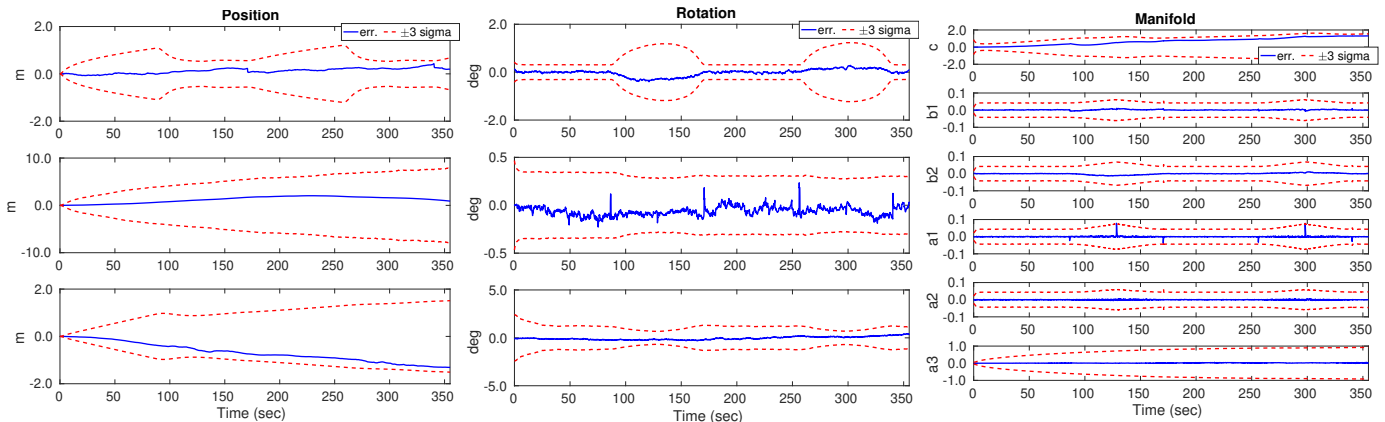


Fig. 5: Estimation errors and the corresponding estimated  $\pm 3\sigma$  curves. The left image corresponds to 3D position, middle one to 3D rotation, and the right one to the motion manifold parameters.

TABLE I: Simulation results: Pose integration errors for three methods: IMU based integration (IMU method), traditional odometry integration (Trad. Odom.), and the proposed manifold based integration (Mani. Odom.).

Integ. Time	0.1 sec	1.0 sec	3.0 sec	5.0 sec	10.0 sec
<b>IMU method</b>					
pos. err. (m)	0.0027	0.0093	0.0544	0.1695	0.9329
rot. err. (deg.)	0.0249	0.0794	0.1450	0.1975	0.2863
<b>Trad. Odom.</b>					
pos. err. (cm)	0.0028	0.0260	0.1899	0.5116	2.1637
rot. err. (deg.)	0.0701	0.6856	1.9715	3.2468	6.8433
<b>Mani. Odom.</b>					
pos. err. (m)	0.0026	0.0086	0.0225	0.0372	0.0688
rot. err. (deg.)	0.0205	0.0646	0.1221	0.1530	0.1621

we are able to test the accuracy of the proposed method for approximating road conditions with locally quadratic equations.

In the tests, simulated odometry, IMU, and camera measurements were generated at 100 Hz, 100 Hz, and 10 Hz respectively. Extrinsic parameters between sensors are assumed to be rigidly fixed, and intrinsic parameters of sensors are assumed to be perfectly calibrated. To obtain camera measurements efficiently, we directly generated feature measurements for each image, with simulated 3D feature positions and known data association. We generated 400 feature points per image on average, and average feature track length is about 5.1 frames. Sensor noises used in the simulation tests match those used in the real-world experiments. During the simulations, the robot was firstly kept static for 1 second, and then started to accelerate with constant linear acceleration  $a = 1m/s$  up to  $3.5m/s$ . After that, the local velocity of the robot was kept as  $3.5m/s$  for the remaining of the simulation trajectories, while its corresponding values in global frame still continuously changed along with the changes with the robot orientation.

1) *Pose Integration Tests*: The first test is to demonstrate the accuracy of pose integration by using the proposed methods. Specifically, we compare the proposed manifold-based integration methods against the widely used IMU-based pose integration [12] [13] and traditional planar-scene based

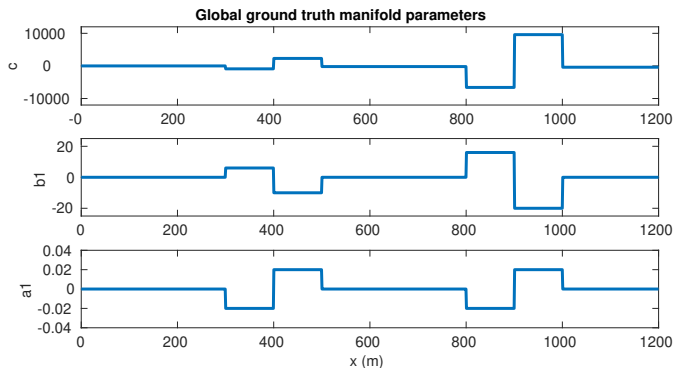


Fig. 6: Ground truth global manifold parameters used for generating simulation trajectories. Only non-zero elements are plotted, while  $b_2$ ,  $a_2$ , and  $a_3$  are constantly zero in this piecewise polynomial test.

odometry integration [6] [21]. All methods started to perform pose integration with perfectly known initial pose and noise-corrupted sensor measurements, for different time durations. In this test, since we focus on 6D odometry integration in this paper, the integration was performed in regions where non-planar slopes exist in top plot of Fig. 4. Table I shows the computed position and rotation errors of the last integrated pose for different methods. Those results show that the by explicitly incorporating manifold equations into the odometry integration process, the accuracy can be largely improved. On the other hand, the accuracy of short-term IMU integration is comparable with our proposed method, while long-term IMU integration becomes not reliable. This verifies our theoretical analysis that the accelerometer measures second-order derivative of poses, and thus errors in IMU integration accumulates faster. Thus, if equipped, odometry should be a preferred proprioceptive sensor used for localizing robots.

2) *Localization Tests*: The second test is to demonstrate the overall localization performance of the proposed method. Specifically, we implemented seven algorithms in this test. Those are a) the standard proposed method using odometry

TABLE II: Simulation results: Localization errors for different methods.

Algorithm	Proposed	Proposed w. IMU	Proposed w/o Re-param.	VIO [15]	VINS-Wheel [21]	[24]	[24] w. IMU
<b>Piece-wise Env.</b>							
Position error (m)	1.043	0.323	11.321	16.400	5.622	11.349	0.673
Rotation error (deg)	0.246	0.099	1.719	0.115	0.323	1.724	0.109
<b>Sinusoidal Env.</b>							
Position error (m)	0.663	0.389	78.335	1.695	13.097	2.512	0.422
Rotation error (deg)	0.066	0.057	25.665	0.071	0.117	0.359	0.090

and camera measurements, b) the proposed method by incorporating additional IMU measurements, c) the proposed method without performing manifold re-parameterization, d) standard visual-inertial odometry [15], e) the VINS-Wheel [21] representing the current state-of-the-art method of fusing measurements from a monocular camera, the wheel odometry, and an IMU, f) our previous work [24] without using IMU, and finally g) [24] with IMU. For all different methods, we compute root-mean-squared-errors (RMSEs) for both 3D position estimates and 3D rotation estimates, which are shown in Table II.

A couple of conclusions can be made from the results. Firstly, our proposed method is able to obtain high-precision localization results even without using IMUs. This is not achievable by other competing methods and our previous work. In fact, the accuracy of the proposed method is even better than a couple of competing methods that employ an IMU sensor. Secondly, when an IMU is also used in localization, the proposed method yields the best performance among algorithms tested. This result indicates that the proposed method is the most preferred one for conducting high-precision localization. Thirdly, we also noticed that when manifold re-parameterization is not used the errors increase significantly. This validates our theoretical analysis in Sec. IV-C that the re-parameterization is a necessary step to ensure manifold propagation errors can be characterized statistically. Finally, it is also important to note that, the proposed methods outperform competing methods also under sinusoidal manifold. This is due to the fact that our quadratic representation of motion manifold is effectively locally within each sliding window, and thus it is able to approximate complex real-scenarios without having large modeling errors. We also note that, when used in the first simulation environment, the estimation errors of VIO are large. This is due to its theoretical drawback of having extra un-observable space under constant-velocity straight-line motion [12]. Since this type of motion is common for ground robot, adding the odometry sensor for localization becomes important.

Additionally, we also plotted the estimation errors and the corresponding uncertainty ellipses for 3D position, 3D rotation, and manifold parameters of the proposed methods in a representative run in Fig. 4. The most important observation from Fig. 4 is that the manifold parameters can be accurately estimated and the estimation errors are well characterized by their uncertainties curves. Additionally, we also noticed that there are two ‘circle’ style curves in the uncertainty ellipses in the top sub-plot of the orientation figure. In fact, those are corresponding to the regions when the ground robot was

climbing (see top one in Fig. 4). This indicates the correctness of the proposed method in Jacobian computation during the pose integration which allows orientation errors to take the changes of manifold parameters into account. Finally, we also point out that both positional and rotational estimates are well characterized by the corresponding uncertainty ellipses in the proposed methods, which indicates the correctness of our mathematical estimator design.

## B. Real-World Experiments

1) *Testing Platforms and Localization Environment:* To evaluate the performance of our proposed approach, we conducted experiments by using datasets from both our customized sensor platform as well as the ones that are publicly available.

Specifically, our sensor platform consists of a stereo camera system with ON AR0144 imaging sensors, a Bosch BMI 088 IMU, and wheel encoders. For our proposed algorithms, only the left eye of the stereo camera system was used, while the full stereo cameras were used for selective competing algorithms. During our data collection, images were recorded at 10Hz with  $640 \times 400$ -pixels resolution, IMU measurements were at 200Hz, and wheel odometer measurements were at 100Hz. Our datasets were all collected on the Yuquan campus of Zhejiang university, Hangzhou, China. This campus is located next to the West Lake in Hangzhou, embraced by mountains on three sides. Therefore, the environments in our datasets are complicated, including frequent slope changes and terrain condition changes.

In addition, we also carried out tests using dataset sequences from the publicly available KAIST dataset [19], which was collected by ground vehicles in different cities in South Korean. The sensors used in our experiment were the left camera of the equipped Pointgrey Flea3 stereo system, the Xsens MTi-300 IMU, and the RLS LM13 wheel encoders. The measurements recorded by those sensors were 10Hz, 100Hz, and 100Hz respectively.

In terms of performance evaluation, we used both the positional final drift and RME error to represent the localization accuracy. For the dataset collected by our platform, due to lack of full-trajectory ground truth, we dedicatedly started and ended our data collection process at exactly the same position, which enables computing the final drift. On the other hand, ground truth poses for the KAIST dataset [19] are available, and we used that for qualitative performance evaluation by computing RMS errors.

2) *Evaluation of Manifold Representation:* The first experiment is to evaluate the necessity and performance of



Fig. 7: Representative visualization of outdoor experiment scenario.

TABLE III: Localization errors of different motion manifold representation methods: using 0th-order, 1st-order, 2nd-order (proposed) representation, and the one without modeling the manifold.

	2nd-order	1st-order	0th-order	w/o manifold
<b>Dataset 01</b>				
pos. err. (m)	<b>0.4993</b>	3.7528	3.2917	2.1186
rot. err. (deg.)	<b>2.78423</b>	3.8094	4.22689	2.95411
<b>Dataset 02</b>				
pos. err. (m)	<b>0.7330</b>	2.6927	2.3419	2.3178
rot. err. (deg.)	<b>2.59439</b>	4.32612	4.44717	3.51778

manifold representation. Specifically, we implemented the proposed localization algorithm in four different modes: 1) removing manifold constraint in Eq. 57, 2) using zero-order approximation for motion manifold (only using  $c$  in Eq. 4), 3) using first-order approximation (using  $c$ ,  $b_1$ , and  $b_2$  in Eq. 4), and 4) using the proposed quadratic representation.

Table III shows localization errors for four different modes, evaluated by two different datasets collected by our sensor platform. A couple of conclusions can be made from the results. First, by using ‘poor’ parameterization for motion manifold, the localization accuracy can even be reduced. In fact, when approximated by zero-th order or first order polynomials, using motion manifold for localization will be worse than not using it. This is due to the fact that outdoor environment is typically complicated and simple representation is not enough. However, when proper modeling (i.e. the proposed method) is used, better localization precision can be achieved. This experiment validates the most important assumption in our paper: with properly designed motion manifold representation the localization accuracy can be improved. In fact, for the two datasets involved, the improvement of position precision is at least 76%, which is significant. We also note that, if a motion manifold is approximated by a polynomial which is less than *second* order, the proposed manifold based 6D integration will be equivalent to *planar* surface 3D integration, and the accuracy will be inevitably reduced.

### 3) Ground Robot Localization in a University Campus:

The next experiment is to evaluate the overall localization performance of the proposed method, compared to representative state-of-the-art algorithms, i.e., hybrid-MSCKF [15], OKVIS-

Stereo [32], VINS-Mono [13], and our previous work [24]. Evaluation were conducted on five datasets, and selective images are shown in Fig. 7. Similar to the previous experiment, the final errors were computed as the metric for different methods. To ensure fair comparison, all algorithms were tested without performing loop closure.

Table IV shows the localization errors for all methods in all testing datasets, the proposed method clearly achieves the best performance. In addition, similar to our simulation tests, those results show that when an IMU is used as an additional sensor for localization, the performance of the proposed algorithm can be further improved. We also note that, the *explicit* manifold cost function introduced in Sec. V-D is important to ensure the poses in the sliding window to be consistently constrained by the manifold equations. If this is not implemented, as shown in Table IV, the performance is reduced. Finally, we emphasize that, by imposing additional kinematic constraints and using additional odometry sensors, the proposed algorithm outperforms competing algorithms for localizing ground robots. Those are theoretically expected results, since the competing algorithms are not dedicatedly designed for ground robots.

### 4) Large-scale Urban Localization for Ground Vehicles:

In addition to the ground robot tests, we also conducted real-world tests on ground vehicles in large-scale urban environments with KAIST dataset [19]. In our tests, we selected 4 dataset sequences, i.e., urban26, urban28, urban38, and urban39. Representative figures recorded in those datasets are shown in Fig. 9. The traveled trajectory lengths for those sequences are 4.00km, 11.47km, 11.42km, and 11.06km respectively. The proposed algorithms (with and without using an IMU), our previous work [24], and a representative visual-inertial navigation algorithm [15] are tested. The qualitative positional RMS errors are shown in Table V, and representative visualization of estimated trajectories on Google maps are shown in Fig. 8. From both Table V and Fig. 8 we can observe that the proposed algorithm is able to provide accurate motion estimates, whose positional RMS errors are always less than 0.38% over traveled distances in all cases. In addition, as we described in previous sections, when an IMU sensor is used, the localization accuracy can be further improved. In comparison, pose estimates from [24] and [15] are consistently

TABLE IV: Position errors of different localization algorithms: the proposed algorithm with IMU, the proposed algorithm without IMU, the proposed algorithm without explicit manifold cost function, hybrid-MSCKF [15], OKVIS-Stereo [32], VINS-Mono[13], and our previous work [24].

	Proposed w. IMU	Proposed	Proposed w/o manifold	[24]	[15]	[32]	[13]
<b>SEQ 01</b>							
pos. err. (m)	1.7804	1.9006	2.2940	<b>1.1568</b>	1.9558	6.8209	7.3542
<b>SEQ 02</b>							
pos. err. (m)	<b>3.3028</b>	5.7115	6.6152	3.8500	5.4742	9.0312	8.5520
<b>SEQ 03</b>							
pos. err. (m)	<b>2.0334</b>	2.8503	11.5017	2.7974	3.4796	6.4802	—
<b>SEQ 04</b>							
pos. err. (m)	<b>2.4266</b>	3.6845	7.6708	2.9968	4.2742	6.3461	6.0619
<b>SEQ 05</b>							
pos. err. (m)	<b>1.8863</b>	3.5367	47.9063	2.7326	5.8041	16.1742	21.5830

<sup>a</sup> —: Fails due to severe drift.

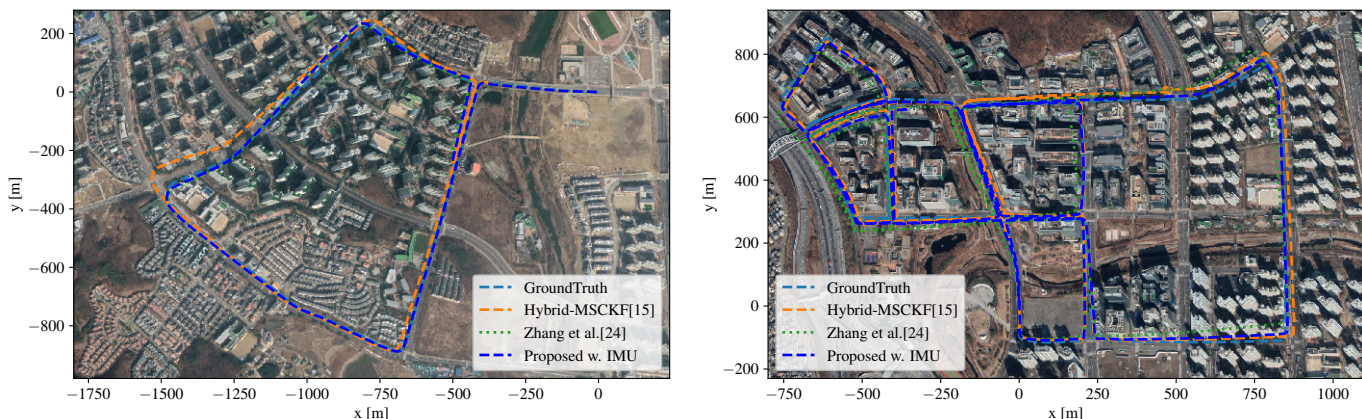


Fig. 8: Ground truth and estimated trajectories of different approaches plotted on Google map. The cyan dashed line corresponds to ground truth trajectory, orange dashed line to estimated one from Hybrid-MSCKF [15], green dotted one to [24], and finally blue dashed one to the proposed method. The left figure shows the results from dataset urban26-dongtan and the right one from urban39-pankyo.



Fig. 9: Representative images recorded from the left eye of the PointGrey camera in KAIST dataset [19].

worse than the proposed methods, even measurements from an IMU is always used. This validates our theoretical analysis that by properly modeling and using the motion manifold, the localization errors can be clearly reduced.

5) *Re-localization Tests*: Lastly, we evaluated our proposed persistent re-localization algorithm proposed in V-F. One a localization map is pre-computed, real-time localization with the given map is typically of high accuracy with bounded

TABLE V: Position RMS errors as well as the corresponding percentage over the trajectory lengths for selective KAIST dataset sequences, using different competing methods.

	Proposed w. IMU	Proposed	[24]	[15]
<b>urban26</b>				
Pos. Err. (m)	14.8115	36.208	16.0557	32.8298
Err. Per. (%)	0.3703	0.9052	0.4014	0.8207
<b>urban28</b>				
Pos. Err. (m)	24.9523	29.2561	33.0718	34.7099
Err. Per. (%)	0.2175	0.2551	0.2883	0.3026
<b>urban38</b>				
Pos. Err. (m)	33.5094	42.0267	42.9578	55.5031
Err. Per. (%)	0.2934	0.3680	0.3762	0.4860
<b>urban39</b>				
Pos. Err. (m)	21.3442	26.2266	24.0151	33.4355
Err. Per. (%)	0.1930	0.2371	0.2171	0.3023

errors. Our motivation of this test is to show that, by using the proposed algorithm with the introduced manifold operations, the accuracy can be further improved.

This test was conducted by using our customized sensor platform, and the localization map was computed using a method similar to [31]. Two methods were tested in this ex-

periment, the proposed method and the one without modeling and using the motion manifold. We also note that, since we focus on persistent re-localization in this test, final drift is not a proper metric for evaluation. In stead, we computed full bundle-adjustment using measurements from both an IMU and cameras, to provide ‘approximate’ ground truth trajectories for computing RMS errors.

The results are shown in Fig. 10, which clearly demonstrate that with the proposed manifold representation the re-localization errors can also be largely reduced, in both positional and rotational elements. Those results indicate that, our proposed algorithm is generic, which can be applied to *different* localization tasks, with and without maps.

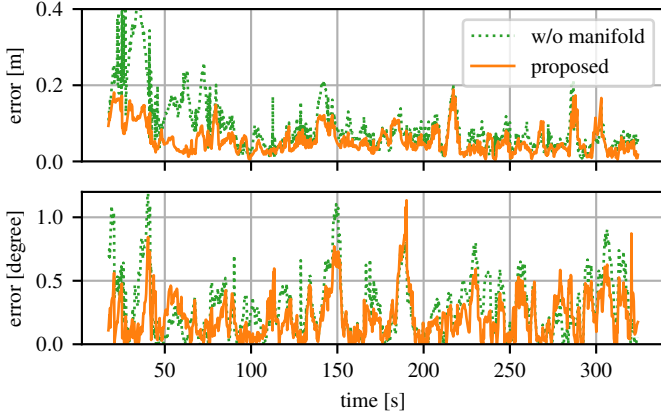


Fig. 10: Translation error and rotation error of two competing algorithms: the proposed one and the one without manifold representation.

## VII. CONCLUSIONS

In this paper, we proposed a high-precision vision-aided localization algorithm dedicatedly designed for ground robots. Since ground robots typically navigates on a local motion manifold, it is possible to exploit this fact to derive kinematic constraints and use proper low-cost sensors in localization algorithms. Specifically, we explicitly modeled the motion manifold by continuously differentiable parametric representation. Subsequently, we proposed a method for performing full 6D pose integration using both wheel odometry measurements and motion manifold in closed-form. We also analyzed the localization errors caused by the manifold representation, and described an algorithm for periodically re-parameterization to achieve error reduction. Finally, we introduced an optimization-based sliding window estimator for fusing measurements from a monocular camera, wheel odometry, and optionally an IMU. By extensive experiments conducted from both simulated and real-world data, we show that the proposed method outperforms competing state-of-the-art localization algorithms by a significant margin.

### APPENDIX A

#### DERIVATIVE OF ORIENTATION ERROR STATE

In this section, we describe the detailed derivation of the orientation error state differential equation, i.e., Eq. 35. To

start with, we substitute Eq. 34 into Eq. 5, which leads to:

$$\frac{\partial \left( \mathbf{G} \hat{\mathbf{R}} (\mathbf{I} + [\delta \boldsymbol{\theta}]) \right)}{\partial t} = \mathbf{G} \hat{\mathbf{R}} (\mathbf{I} + [\delta \boldsymbol{\theta}]) [{}^{\mathbf{O}} \boldsymbol{\omega}] \quad (67)$$

$$\Rightarrow \mathbf{G} \hat{\mathbf{R}} [{}^{\mathbf{O}} \hat{\boldsymbol{\omega}}] (\mathbf{I} + [\delta \boldsymbol{\theta}]) + \mathbf{G} \hat{\mathbf{R}} [\dot{\delta \boldsymbol{\theta}}] = \mathbf{G} \hat{\mathbf{R}} (\mathbf{I} + [\delta \boldsymbol{\theta}]) [{}^{\mathbf{O}} \hat{\boldsymbol{\omega}} + {}^{\mathbf{O}} \tilde{\boldsymbol{\omega}}] \quad (68)$$

$$\Rightarrow [{}^{\mathbf{O}} \hat{\boldsymbol{\omega}}] (\mathbf{I} + [\delta \boldsymbol{\theta}]) + [\dot{\delta \boldsymbol{\theta}}] = (\mathbf{I} + [\delta \boldsymbol{\theta}]) [{}^{\mathbf{O}} \hat{\boldsymbol{\omega}} + {}^{\mathbf{O}} \tilde{\boldsymbol{\omega}}] \quad (69)$$

By applying the quadratic error approximation  $[\delta \boldsymbol{\theta}] [{}^{\mathbf{O}} \tilde{\boldsymbol{\omega}}] \simeq \mathbf{0}$ , the above equation can be written as:

$$[\dot{\delta \boldsymbol{\theta}}] \simeq (\mathbf{I} + [\delta \boldsymbol{\theta}]) [{}^{\mathbf{O}} \hat{\boldsymbol{\omega}} + {}^{\mathbf{O}} \tilde{\boldsymbol{\omega}}] - [{}^{\mathbf{O}} \hat{\boldsymbol{\omega}}] (\mathbf{I} + [\delta \boldsymbol{\theta}]) \quad (70)$$

$$\simeq [\delta \boldsymbol{\theta}] [{}^{\mathbf{O}} \hat{\boldsymbol{\omega}}] - [{}^{\mathbf{O}} \hat{\boldsymbol{\omega}}] [\delta \boldsymbol{\theta}] + [{}^{\mathbf{O}} \tilde{\boldsymbol{\omega}}] \quad (71)$$

Finally, by using the property of skew-symmetric matrix:

$$[\mathbf{a}] [\mathbf{b}] - [\mathbf{b}] [\mathbf{a}] = \mathbf{b} \mathbf{a}^T - \mathbf{a} \mathbf{b}^T = [[\mathbf{a}] \mathbf{b}] = -[[\mathbf{b}] \mathbf{a}] \quad (72)$$

Eq. 71 becomes:

$$\dot{\delta \boldsymbol{\theta}} = -[{}^{\mathbf{O}} \hat{\boldsymbol{\omega}}] \delta \boldsymbol{\theta} + {}^{\mathbf{O}} \tilde{\boldsymbol{\omega}} \quad (73)$$

and

$${}^{\mathbf{O}} \tilde{\boldsymbol{\omega}} = \mathbf{J}_x \tilde{x} + \mathbf{J}_n \mathbf{n}_\omega \quad (74)$$

This completes the derivation.

### APPENDIX B

#### JACOBIAN OF THE INFERRED ANGULAR VELOCITY

In this section, we describe the detailed derivation of Jacobians in Eq. 35. Recall the inferred local angular velocity in Eq. 18:

$${}^{\mathbf{O}}(t) \hat{\boldsymbol{\omega}} = \begin{bmatrix} \frac{1}{\|\nabla \hat{\mathcal{M}}(t)\|} \mathbf{e}_{12}^T [\mathbf{e}_3] (\mathbf{G}_{\mathbf{O}(t)} \hat{\mathbf{R}}^T \cdot \nabla \hat{\mathcal{M}}(t)) \\ \omega_{\mathbf{O}}(t) \end{bmatrix} \quad (75)$$

where  $\nabla \hat{\mathcal{M}}(t)$  and  $\nabla \dot{\hat{\mathcal{M}}}(t)$  represent the gradient and its time derivative of the equality manifold constraint evaluated at current state estimate. Based on Eq. 2, we can derive:

$$\nabla \mathcal{M} = \begin{bmatrix} \mathbf{A} \begin{bmatrix} \mathbf{G} \mathbf{p}_{\mathbf{O}_x} \\ \mathbf{G} \mathbf{p}_{\mathbf{O}_y} \\ 1 \end{bmatrix} + \mathbf{B} \\ \mathbf{0} \end{bmatrix}, \quad \nabla \dot{\mathcal{M}} = \begin{bmatrix} \mathbf{A} \begin{bmatrix} \mathbf{G} v_x \\ \mathbf{G} v_y \\ 0 \end{bmatrix} \\ \mathbf{0} \end{bmatrix} \quad (76)$$

or equivalently:

$$\nabla \mathcal{M} = \bar{\mathbf{A}} \mathbf{G} \mathbf{p}_{\mathbf{O}} + \bar{\mathbf{B}} + \mathbf{e}_3, \quad \nabla \dot{\mathcal{M}} = \bar{\mathbf{A}} \mathbf{G} \mathbf{v}_{\mathbf{O}}, \quad \bar{\mathbf{A}} = \begin{bmatrix} \mathbf{A} & \mathbf{0} \\ \mathbf{0}^T & \mathbf{0} \end{bmatrix}, \quad \bar{\mathbf{B}} = \begin{bmatrix} \mathbf{B} \\ \mathbf{0} \end{bmatrix} \quad (77)$$

By denoting  $\mathbf{E} = \mathbf{e}_{12}^T [\mathbf{e}_3]$ ,  $\mathbf{D} = \mathbf{G}_{\mathbf{O}} \mathbf{R} \cdot \bar{\mathbf{A}} \cdot \mathbf{G}_{\mathbf{O}} \mathbf{R}^T$  and dropping  $(t)$  for simplicity, we write Eq. 18 as:

$${}^{\mathbf{O}} \boldsymbol{\omega} = \begin{bmatrix} \frac{1}{\|\nabla \mathcal{M}\|} \mathbf{E} \mathbf{D} (\mathbf{O} \mathbf{v} - \mathbf{n}_v) \\ \omega_{\mathbf{O}} - n_{\omega_{\mathbf{O}}} \end{bmatrix} \quad (78)$$

To compute the state-transition matrix, we first note that:

$$\begin{aligned} \frac{\partial \|\mathbf{y}\|}{\partial \mathbf{y}} &= \frac{\mathbf{y}^T}{\|\mathbf{y}\|}, & \frac{\partial \frac{1}{\|\mathbf{y}\|}}{\partial \mathbf{y}} &= -\frac{\mathbf{y}^T}{\|\mathbf{y}\|^3}, \quad \text{and} \\ \frac{\partial \frac{\mathbf{k}}{\|\mathbf{y}\|}}{\partial \mathbf{y}} &= -\frac{\mathbf{k} \mathbf{y}^T}{\|\mathbf{y}\|^3}, & \frac{\partial \frac{\mathbf{k}}{\|\mathbf{y}\|}}{\partial \mathbf{x}} &= -\frac{\mathbf{k} \mathbf{y}^T}{\|\mathbf{y}\|^3} \frac{\partial \mathbf{y}}{\partial \mathbf{x}} \end{aligned} \quad (79)$$

By employing Eq. 79, we have:

$$\frac{\partial^{\mathcal{O}}\boldsymbol{\omega}}{\partial^{\mathcal{G}}\mathbf{p}_o} = \begin{bmatrix} -\mathbf{E}\hat{\mathbf{D}}\mathbf{e}_1v_o \frac{\nabla\hat{\mathcal{M}}^T}{\|\nabla\hat{\mathcal{M}}\|^3}\bar{\mathbf{A}} \\ \mathbf{0} \end{bmatrix} \quad (80)$$

and

$$\frac{\partial^{\mathcal{O}}\boldsymbol{\omega}}{\partial\delta\boldsymbol{\theta}} = \begin{bmatrix} \frac{\mathbf{E}}{\|\nabla\hat{\mathcal{M}}\|} \cdot \left( [\hat{\mathbf{D}}\mathbf{e}_1v_o] - \hat{\mathbf{D}}[\mathbf{e}_1v_o] \right) \\ \mathbf{0} \end{bmatrix} \quad (81)$$

finally

$$\frac{\partial^{\mathcal{O}}\boldsymbol{\omega}}{\partial\mathbf{m}} = \begin{bmatrix} -\mathbf{E}\hat{\mathbf{D}}\mathbf{e}_1v_o \frac{\nabla\hat{\mathcal{M}}^T}{\|\nabla\hat{\mathcal{M}}\|^3}\hat{\boldsymbol{\Gamma}} + \frac{\mathbf{E}}{\|\nabla\hat{\mathcal{M}}\|}\mathbf{G}\hat{\mathbf{R}}\hat{\boldsymbol{\Upsilon}} \\ \mathbf{0} \end{bmatrix} \quad (82)$$

with

$$\boldsymbol{\Gamma} = \begin{bmatrix} 0 & 1 & 0 & \mathbf{G}\mathbf{p}_{o_x} & \mathbf{G}\mathbf{p}_{o_y} & 0 \\ 0 & 0 & 1 & 0 & \mathbf{G}\mathbf{p}_{o_x} & \mathbf{G}\mathbf{p}_{o_y} \\ 0 & 0 & 0 & 0 & 0 & 0 \end{bmatrix} \quad (83)$$

and

$$\boldsymbol{\Upsilon} = \begin{bmatrix} 0 & 0 & 0 & \mathbf{G}\mathbf{v}_{o_x} & \mathbf{G}\mathbf{v}_{o_y} & 0 \\ 0 & 0 & 0 & 0 & \mathbf{G}\mathbf{v}_{o_x} & \mathbf{G}\mathbf{v}_{o_y} \\ 0 & 0 & 0 & 0 & 0 & 0 \end{bmatrix} \quad (84)$$

To summarize the Jacobians with respect to the state, we have:

$$\mathbf{J}_x = \begin{bmatrix} \frac{\partial^{\mathcal{O}}\boldsymbol{\omega}}{\partial^{\mathcal{G}}\mathbf{p}_o} & \frac{\partial^{\mathcal{O}}\boldsymbol{\omega}}{\partial\delta\boldsymbol{\theta}} & \frac{\partial^{\mathcal{O}}\boldsymbol{\omega}}{\partial\mathbf{m}} \end{bmatrix} \quad (85)$$

On the other hand,  $\mathbf{J}_n$  can be easily computed by taking derivative with respect to  $\mathbf{n} = [n_{v_o} \ n_{\omega_o}]^T$ .

$$\mathbf{J}_n = - \begin{bmatrix} \frac{1}{\|\nabla\hat{\mathcal{M}}\|}\mathbf{E}\hat{\mathbf{D}}\mathbf{e}_1 & \mathbf{0}_{2 \times 1} \\ 0 & 1 \end{bmatrix} \quad (86)$$

## APPENDIX C

### DERIVATION ON MANIFOLD RE-PARAMETERIZATION

In this section, we provide the detailed derivations of Eq. 49. To simplify our analysis, we here use  $\mathbf{m}_o = \mathbf{m}(t_k)$  and  $\mathbf{m}_1 = \mathbf{m}(t_{k+1})$  for abbreviation. In our work, we define the local manifold representation at  $t_k$  and  $t_{k+1}$  as:

$$z + c + \mathbf{B}^T \mathbf{v}_o + \frac{1}{2} \mathbf{v}_o^T \mathbf{A} \mathbf{v}_o = 0, \quad \mathbf{v}_o = \mathbf{R}_o \left( \begin{bmatrix} x \\ y \end{bmatrix} - \begin{bmatrix} x_o \\ y_o \end{bmatrix} \right) \quad (87)$$

$$z + c + \mathbf{B}^T \mathbf{v}_1 + \frac{1}{2} \mathbf{v}_1^T \mathbf{A} \mathbf{v}_1 = 0, \quad \mathbf{v}_1 = \mathbf{R}_1 \left( \begin{bmatrix} x \\ y \end{bmatrix} - \begin{bmatrix} x_1 \\ y_1 \end{bmatrix} \right) \quad (88)$$

where  $\mathbf{x}_o^T = [x_o \ y_o]$  and  $\mathbf{x}_1^T = [x_1 \ y_1]$ , and the detailed formulation of  $\mathbf{A}$  and  $\mathbf{B}$  can be found in Eq. 3 - Eq. 4. We note that, Eq. 87 - 88 should hold for all  $\mathbf{x}$ , and thus the corresponding coefficients for  $\mathbf{x}$  should be the same in both equations. Considering the equality on the second order coefficients leads to:

$$\mathbf{R}_o^T \mathbf{A} \mathbf{R}_o = \mathbf{R}_1^T \mathbf{A}_{new} \mathbf{R}_1 \quad (89)$$

$$\Rightarrow \mathbf{A}_{new} = \delta \mathbf{R}^T \mathbf{A} \delta \mathbf{R}, \quad \text{with } \delta \mathbf{R} = \mathbf{R}_o \mathbf{R}_1^{-1} \quad (90)$$

and the first order ones:

$$\mathbf{B}^T \mathbf{R}_o - \mathbf{x}_o^T \mathbf{R}_o^T \mathbf{A} \mathbf{R}_o = \mathbf{B}_{new}^T \mathbf{R}_1 - \mathbf{x}_1^T \mathbf{R}_1^T \mathbf{A}_{new} \mathbf{R}_1 \quad (91)$$

$$\Rightarrow \mathbf{B}_{new}^T = \mathbf{B}^T \delta \mathbf{R} - \mathbf{x}_o^T \mathbf{R}_o^T \mathbf{A} \delta \mathbf{R} + \mathbf{x}_1^T \mathbf{R}_1^T \mathbf{A} \delta \mathbf{R} \quad (92)$$

$$\Rightarrow \mathbf{B}_{new} = \delta \mathbf{R}^T \mathbf{B} + \delta \mathbf{R}^T \mathbf{A}^T \delta \mathbf{x}, \quad \text{with } \delta \mathbf{x} = \mathbf{R}_o (\mathbf{x}_1 - \mathbf{x}_o) \quad (93)$$

finally the constant value:

$$c - \mathbf{B}^T \mathbf{R}_o \mathbf{x}_o + \frac{1}{2} \mathbf{x}_o^T \mathbf{R}_o^T \mathbf{A} \mathbf{R}_o \mathbf{x}_o = c_{new} - \mathbf{B}_{new}^T \mathbf{R}_1 \mathbf{x}_1 + \frac{1}{2} \mathbf{x}_1^T \mathbf{R}_1^T \mathbf{A}_{new} \mathbf{R}_1 \mathbf{x}_1 \quad (94)$$

$$\Rightarrow c_{new} = c + \mathbf{B}^T \delta \mathbf{R} \mathbf{R}_1 \mathbf{x}_1 + (\mathbf{x}_1 - \mathbf{x}_o)^T \mathbf{R}_o^T \mathbf{A} \delta \mathbf{R} \mathbf{R}_1 \mathbf{x}_1 - \mathbf{B}^T \mathbf{R}_o \mathbf{x}_o - \frac{1}{2} \mathbf{x}_1^T \mathbf{R}_o^T \mathbf{A} \mathbf{R}_o \mathbf{x}_1 + \frac{1}{2} \mathbf{x}_o^T \mathbf{R}_o^T \mathbf{A} \mathbf{R}_o \mathbf{x}_o \quad (95)$$

$$\Rightarrow c_{new} = c + \mathbf{B}^T \delta \mathbf{x} + \frac{1}{2} \delta \mathbf{x}^T \mathbf{A} \delta \mathbf{x} \quad (96)$$

In matrix form representation, we have:

$$\mathbf{m}_{new} = \underbrace{\begin{bmatrix} 1 & \delta \mathbf{x}^T & \boldsymbol{\gamma}^T \\ \mathbf{0} & \delta \mathbf{R}^T & \boldsymbol{\Xi} \\ \mathbf{0} & \mathbf{0} & \boldsymbol{\Psi} \end{bmatrix}}_{\Lambda_1} \mathbf{m} \quad (97)$$

with

$$\boldsymbol{\gamma}^T = [0.5\delta x^2 \quad \delta x \delta y \quad 0.5\delta y^2], \quad \boldsymbol{\Xi} = \delta \mathbf{R}^T \begin{bmatrix} \delta x & \delta y & 0 \\ 0 & \delta x & \delta y \end{bmatrix} \quad (98)$$

and

$$\boldsymbol{\Psi} = \begin{bmatrix} \delta r_1^2 & 2\delta r_1 \delta r_3 & \delta r_3^2 \\ \delta r_1 \delta r_2 & \delta r_1 \delta r_4 + \delta r_2 \delta r_3 & \delta r_3 \delta r_4 \\ \delta r_2^2 & 2\delta r_2 \delta r_4 & \delta r_4^2 \end{bmatrix}, \quad \delta \mathbf{R} = \begin{bmatrix} \delta r_1 & \delta r_2 \\ \delta r_3 & \delta r_4 \end{bmatrix} \quad (99)$$

This completes our derivation.

We next discuss the choices of parameters in  $\mathbf{x}_o$ ,  $\mathbf{x}_1$ ,  $\mathbf{R}_o$ , and  $\mathbf{R}_1$ . As described earlier in Sec. IV-C, we choose the *first* estimate of  $\mathbf{G}\mathbf{p}_{o(t_k)}$  for  $\mathbf{x}_o$  and  $\mathbf{G}\mathbf{p}_{o(t_{k+1})}$  for  $\mathbf{x}_1$ . For  $\mathbf{R}_o$  and  $\mathbf{R}_1$ , we've tested two sets of choices, by extracting the corresponding elements in *yaw* of the *first* estimate of  $\mathbf{G}_{O(t_k)} \mathbf{R}^T$  and  $\mathbf{G}_{O(t_{k+1})} \mathbf{R}^T$  or simply  $\mathbf{I}_2$  matrices. Based on our theoretical analysis in Sec. IV-C and experimental results in Sec. VI-A2, we show that our parameter choices in  $\mathbf{x}_o$  and  $\mathbf{x}_1$  are important, resulting in significant performance gain. On the other hand, we find the accuracy of parameter choices in  $\mathbf{R}_o$  and  $\mathbf{R}_1$  is similar among our choices, and thus for the experimental results reported in this work, we use  $\mathbf{I}_2$  matrices as the rotation parameters for the simplicity.

## REFERENCES

- [1] Teddy Yap, Mingyang Li, Anastasios I Mourikis, and Christian R Shelton. A particle filter for monocular vision-aided odometry. In *IEEE International Conference on Robotics and Automation*, 2011.
- [2] Ji Zhang and Sanjiv Singh. Low-drift and real-time lidar odometry and mapping. *Autonomous Robots*, 41(2):401–416, 2017.
- [3] Jesse Levinson, Michael Montemerlo, and Sebastian Thrun. Map-based precision vehicle localization in urban environments. In *Robotics: Science and Systems*, volume 4, page 1, 2007.
- [4] Ryan W Wolcott and Ryan M Eustice. Visual localization within lidar maps for automated urban driving. In *IEEE/RSJ International Conference on Intelligent Robots and Systems*, pages 176–183, 2014.
- [5] Mingming Zhang, Yiming Chen, and Mingyang Li. SDF-loc: Signed distance field based 2D relocalization and map update in dynamic environments. In *American Control Conference*, 2019.
- [6] Andrea Censi, Antonio Franchi, Luca Marchionni, and Giuseppe Oriolo. Simultaneous calibration of odometry and sensor parameters for mobile robots. *IEEE Transactions on Robotics*, 29(2):475–492, 2013.

- [7] Cesar Cadena, Luca Carlone, Henry Carrillo, Yasir Latif, Davide Scaramuzza, José Neira, Ian Reid, and John J Leonard. Past, present, and future of simultaneous localization and mapping: Toward the robust-perception age. *IEEE Transactions on Robotics*, 32(6):1309–1332, 2016.
- [8] Guowei Wan, Xiaolong Yang, Renlan Cai, Hao Li, Yao Zhou, Hao Wang, and Shiyu Song. Robust and precise vehicle localization based on multi-sensor fusion in diverse city scenes. In *IEEE International Conference on Robotics and Automation (ICRA)*, pages 4670–4677, 2018.
- [9] Bryan Klingner, David Martin, and James Roseborough. Street view motion-from-structure-from-motion. In *Proceedings of the IEEE International Conference on Computer Vision*, pages 953–960, 2013.
- [10] Jesse Levinson, Jake Askeland, Jan Becker, Jennifer Dolson, David Held, Soeren Kammel, J Zico Kolter, Dirk Langer, Oliver Pink, Vaughan Pratt, et al. Towards fully autonomous driving: Systems and algorithms. In *Intelligent Vehicles Symposium (IV), 2011 IEEE*, pages 163–168, 2011.
- [11] Raul Mur-Artal, Jose Maria Martinez Montiel, and Juan D Tardos. Orb-slam: a versatile and accurate monocular slam system. *IEEE Transactions on Robotics*, 31(5):1147–1163, 2015.
- [12] Mingyang Li and Anastasios I Mourikis. High-precision, consistent ekf-based visual-inertial odometry. *The International Journal of Robotics Research*, 32(6):690–711, 2013.
- [13] Tong Qin, Peiliang Li, and Shaojie Shen. Vins-mono: A robust and versatile monocular visual-inertial state estimator. *IEEE Transactions on Robotics*, 34(4):1004–1020, 2018.
- [14] Simon Lynen, Torsten Sattler, Michael Bosse, Joel A Hesch, Marc Pollefeys, and Roland Siegwart. Get out of my lab: Large-scale, real-time visual-inertial localization. In *Robotics: Science and Systems*, 2015.
- [15] Mingyang Li and Anastasios I Mourikis. Optimization-based estimator design for vision-aided inertial navigation. In *Robotics: Science and Systems*, pages 241–248, 2013.
- [16] Zheng Huai and Guoquan Huang. Robocentric visual-inertial odometry. In *IEEE/RSJ International Conference on Intelligent Robots and Systems (IROS)*, pages 6319–6326, 2018.
- [17] Haomin Liu, Mingyu Chen, Guofeng Zhang, Hujun Bao, and Yingze Bao. ICE-BA: Incremental, consistent and efficient bundle adjustment for visual-inertial SLAM. In *Proceedings of the IEEE Conference on Computer Vision and Pattern Recognition*, pages 1974–1982, 2018.
- [18] Barza Nisar, Philipp Foehn, Davide Falanga, and Davide Scaramuzza. Vimo: Simultaneous visual inertial model-based odometry and force estimation. *IEEE Robotics and Automation Letters*, 2019.
- [19] Jinyong Jeong, Younggun Cho, Young-Sik Shin, Hyunchul Roh, and Ayoung Kim. Complex urban dataset with multi-level sensors from highly diverse urban environments. *The International Journal of Robotics Research*, 38(6):642–657, 2019.
- [20] Mingyang Li and Anastasios I Mourikis. Online temporal calibration for camera-imu systems: Theory and algorithms. *The International Journal of Robotics Research*, 33(7):947–964, 2014.
- [21] Kejian J Wu, Chao X Guo, Georgios Georgiou, and Stergios I Roumeliotis. VINS on wheels. In *IEEE International Conference on Robotics and Automation (ICRA)*, pages 5155–5162, 2017.
- [22] Dimitrios G Kottas, Kejian J Wu, and Stergios I Roumeliotis. Detecting and dealing with hovering maneuvers in vision-aided inertial navigation systems. In *IEEE/RSJ International Conference on Intelligent Robots and Systems*, pages 3172–3179, 2013.
- [23] Meixiang Quan, Songhao Piao, Minglang Tan, and Shi-Sheng Huang. Tightly-coupled monocular visual-odometric slam using wheels and a mems gyroscope. *arXiv preprint arXiv:1804.04854*, 2018.
- [24] Mingming Zhang, Yiming Chen, and Mingyang Li. Vision-aided localization for ground robots. In *IEEE/RSJ International Conference on Intelligent Robots and Systems (IROS)*, 2019.
- [25] Jingang Yi, Junjie Zhang, Dezhen Song, and Suhada Jayasuriya. IMU-based localization and slip estimation for skid-steered mobile robots. In *IEEE/RSJ International Conference on Intelligent Robots and Systems (IROS)*, pages 2845–2850, 2007.
- [26] T.C. Dong-Si and A. I. Mourikis. Consistency analysis for sliding-window visual odometry. In *Proceedings of the IEEE International Conference on Robotics and Automation (ICRA)*, Minneapolis, MN, May 2012.
- [27] Jakob Engel, Thomas Schöps, and Daniel Cremers. LSD-SLAM: Large-scale direct monocular slam. In *European conference on computer vision*, pages 834–849, 2014.
- [28] Jakob Engel, Vladlen Koltun, and Daniel Cremers. Direct sparse odometry. *IEEE transactions on pattern analysis and machine intelligence*, 40(3):611–625, 2017.
- [29] Raul Mur-Artal and Juan D Tardós. ORB-SLAM2: An open-source slam system for monocular, stereo, and rgb-d cameras. *IEEE Transactions on Robotics*, 33(5):1255–1262, 2017.
- [30] Christian Forster, Luca Carlone, Frank Dellaert, and Davide Scaramuzza. On-manifold preintegration for real-time visual-inertial odometry. *IEEE Transactions on Robotics*, 33(1):1–21, 2017.
- [31] Thomas Schneider, Marcin Dymczyk, Marius Fehr, Kevin Egger, Simon Lynen, Igor Gilitschenski, and Roland Siegwart. maplab: An open framework for research in visual-inertial mapping and localization. *IEEE Robotics and Automation Letters*, 3(3):1418–1425, 2018.
- [32] Stefan Leutenegger, Simon Lynen, Michael Bosse, Roland Siegwart, and Paul Furgale. Keyframe-based visual-inertial odometry using nonlinear optimization. *The International Journal of Robotics Research*, 34(3):314–334, 2015.
- [33] Xiao Chen, Weidong Hu, Lefeng Zhang, Zhiguang Shi, and Maisi Li. Integration of low-cost gnss and monocular cameras for simultaneous localization and mapping. *Sensors*, 18(7):2193, 2018.
- [34] Ji Zhang and Sanjiv Singh. Visual-lidar odometry and mapping: Low-drift, robust, and fast. In *IEEE International Conference on Robotics and Automation (ICRA)*, pages 2174–2181, 2015.
- [35] Mingyang Li and Anastasios I Mourikis. Vision-aided inertial navigation for resource-constrained systems. In *IEEE/RSJ International Conference on Intelligent Robots and Systems (IROS)*, pages 1057–1063, 2012.
- [36] Thomas Schneider, Mingyang Li, Michael Burri, Juan Nieto, Roland Siegwart, and Igor Gilitschenski. Visual-inertial self-calibration on informative motion segments. In *IEEE International Conference on Robotics and Automation (ICRA)*, pages 6487–6494, 2017.
- [37] Ronald Clark, Sen Wang, Andrew Markham, Niki Trigoni, and Hongkai Wen. Vidloc: A deep spatio-temporal model for 6-dof video-clip relocalization. In *Proceedings of the IEEE Conference on Computer Vision and Pattern Recognition*, pages 6856–6864, 2017.
- [38] Michael Bloesch, Jan Czarnowski, Ronald Clark, Stefan Leutenegger, and Andrew J Davison. Codeslamlearning a compact, optimisable representation for dense visual slam. In *Proceedings of the IEEE Conference on Computer Vision and Pattern Recognition*, pages 2560–2568, 2018.
- [39] Olga Russakovsky, Jia Deng, Hao Su, Jonathan Krause, Sanjeev Satheesh, Sean Ma, Zhiheng Huang, Andrej Karpathy, Aditya Khosla, Michael Bernstein, et al. Imagenet large scale visual recognition challenge. *International journal of computer vision*, 115(3):211–252, 2015.
- [40] David Nistér, Oleg Naroditsky, and James Bergen. Visual odometry for ground vehicle applications. *Journal of Field Robotics*, 23(1):3–20, 2006.
- [41] F. Zheng and Y. Liu. Se(2)-constrained visual inertial fusion for ground vehicles. *IEEE Sensors Journal*, Oct. 2018.
- [42] Chenyang Lu, Gijs Dubbelman, and Marinus Jacobus Gerardus van de Molengraft. Monocular semantic occupancy grid mapping with convolutional variational auto-encoders. *CoRR*, 2018.
- [43] Ji Zhang and Sanjiv Singh. Laser-visual-inertial odometry and mapping with high robustness and low drift. *Journal of Field Robotics*, 35(8):1242–1264, 2018.
- [44] Wolfgang Hess, Damon Kohler, Holger Rapp, and Daniel Andor. Real-time loop closure in 2d lidar slam. In *Robotics and Automation (ICRA), 2016 IEEE International Conference on*, pages 1271–1278, 2016.
- [45] Changhao Chen, Xiaoxuan Lu, Andrew Markham, and Niki Trigoni. Ionet: Learning to cure the curse of drift in inertial odometry. *CoRR*, abs/1802.02209, 2018.
- [46] Changhao Chen, Peijun Zhao, Chris Xiaoxuan Lu, Wei Wang, Andrew Markham, and Niki Trigoni. Oxiod: The dataset for deep inertial odometry. *arXiv preprint arXiv:1809.07491*, 2018.
- [47] Boram Lee, Kostas Daniilidis, and Daniel D Lee. Online self-supervised monocular visual odometry for ground vehicles. In *IEEE International Conference on Robotics and Automation (ICRA)*, pages 5232–5238, Seattle, WA, May 2015.
- [48] Nikolas Trawny and Stergios I Roumeliotis. Indirect kalman filter for 3D attitude estimation. 2005.
- [49] Edward Rosten, Reid Porter, and Tom Drummond. Faster and better: A machine learning approach to corner detection. *IEEE transactions on pattern analysis and machine intelligence*, 32(1):105–119, 2008.
- [50] Alexandre Alahi, Raphael Ortiz, and Pierre Vanderghenst. Freak: Fast retina keypoint. In *IEEE Conference on Computer Vision and Pattern Recognition*, pages 510–517, 2012.
- [51] Mingyang Li, Byung Hyung Kim, and Anastasios I Mourikis. Real-time motion tracking on a cellphone using inertial sensing and a rolling-shutter camera. In *IEEE International Conference on Robotics and Automation*, pages 4712–4719, 2013.